JGR Atmospheres

RESEARCH ARTICLE
10.1029/2019JD031026

Key Points:
- Convective organization becomes more frequent throughout the tropics, and especially over warmer ocean waters, during El Niño
- The vertical depth, horizontal extent, and attributable precipitation of tropical organized convection increase during El Niño
- We present new metrics that quantify the relative importance of convective system deepening to spreading and their degree of organization

Supporting Information:
- Supporting Information S1

Correspondence to:
S. C. Sullivan,
scs2229@columbia.edu

Citation:
Sullivan, S. C., Schiro, K. A., Stubenrauch, C., & Gentine, P. (2019). The response of tropical organized convection to El Niño warming. *Journal of Geophysical Research: Atmospheres*, *124*, 8481–8500. https://doi.org/10.1029/2019JD031026

Received 17 MAY 2019
Accepted 11 JUL 2019
Accepted article online 20 JUL 2019
Published online 5 AUG 2019

Author Contributions
Data curation: Claudia Stubenrauch
Funding Acquisition: Pierre Gentine
Methodology: Pierre Gentine
Project Administration: Pierre Gentine
Resources: Claudia Stubenrauch
Supervision: Pierre Gentine
Writing - review & editing: Kathleen A. Schiro, Claudia Stubenrauch, Pierre Gentine

The Response of Tropical Organized Convection to El Niño Warming

Sylvia C. Sullivan[1], **Kathleen A. Schiro**[2], **Claudia Stubenrauch**[3], **and Pierre Gentine**[1]

[1]Department of Earth and Environmental Engineering, Columbia University, New York, NY, USA, [2]Jet Propulsion Laboratory, California Institute of Technology, Pasadena, CA, USA, [3]Laboratoire de Météorologie Dynamique/Institut Pierre-Simon Laplace (LMD/IPSL), CNRS, Sorbonnes Universities, University Pierre and Marie Curie (UPMC) Paris 06, Paris, France

Abstract Convective organization has a large impact on precipitation and feeds back on larger-scale circulations in the tropics. The degree of this convective organization changes with modes of climate variability like the El Niño–Southern Oscillation (ENSO), but because organization is not represented in current climate models, a quantitative assessment of these shifts has not been possible. Here, we construct multidecade satellite climatologies of occurrence of tropical convective organization and its properties and assess changes with ENSO phase. The occurrence of organized deep convection becomes more concentrated, increasing threefold in the eastern and central Pacific during El Niño and decreasing twofold outside of these regions. Both horizontal extent of the cold cloud shield and convective depth increase in regions of positive sea surface temperature anomaly (SSTa); however, the regions of greatest convective deepening are those of large-scale ascent, rather than those of warmest SSTa. Extent decreases with SSTa at a rate of about 20 km/K, while the SSTa dependence of depth is only about 0.2 K/K. We introduce two values to describe convective changes with ENSO more succinctly: (1) an information entropy metric to quantify the clustering of convective system occurrences and (2) a growth metric to quantify deepening relative to spreading over the system lifetime. Finally, with collocated precipitation data, we see that rainfall attributable to convective organization jumps up to 5% with warming. Rain intensity and amount increase for a given system size during El Niño, but a given rain amount may actually fall with higher intensity during La Niña.

Plain Language Summary Tropical storms at an intermediate scale between individual thunderstorms and cyclones or hurricanes are not represented by climate models. As the satellite data record now spans several decades, we can use these observations to understand how large storms change during El Niño periods. Here, we find that warmer waters in the central and eastern Pacific during El Niño cause a dramatic increase in storm occurrence. Storms are more likely to occur near to other storms and to become larger in both the vertical and horizontal. Changes to large-scale winds are more influential on these structural factors than locally warmer ocean water. The hydrological impact of these storms is also important because they bring the majority of precipitation in some regions. We see that a storm of a certain extent brings larger volume and intensity of rain during El Niño. But a certain rain volume may actually fall with greater intensity during La Niño.

1. Introduction

Under the right conditions, individual deep convective cells can develop into larger-scale systems with long lifetimes and self-sustaining circulations. These systems include mesoscale convective systems (MCS), mesoscale convective complexes, and superclusters and are generally characterized by strong vertical motions and intense precipitation in a localized area (Houze, 2004). We define organized convection here as meso-α systems with a cold cloud shield of infrared (IR) brightness temperature 245 K or less over an area of at least 90-km equivalent radius and with at least one convective core of IR brightness temperature 220 K or less, following Machado et al. (1998) and Rossow and Schiffer (1999). This organization can have important radiative and dynamical impacts on climate via outflow cirrus and adjustments to the vertical latent heating profile (Bouniol et al., 2016; Roca et al., 2014; Schumacher et al., 2004), while associated precipitation contributes disproportionately to the tropics-wide accumulation (Nesbitt & Zipser, 2003; Tao &

Chern, 2017). Given their association with flooding, strong winds, and hail, it is important to understand how these systems will adjust to tropical sea surface temperature (SST) gradients during different phases of the El Niño–Southern Oscillation (ENSO), a dominant mode of climate variability.

Many studies have looked at changes in storm occurrence or strength with ENSO or greenhouse warming. Although trends of storm occurrence are less clear, intensification of tropical cyclones and hurricanes is fairly well established (e.g., Emanuel, 2005; Held & Zhao, 2011; Knutson & Tuleya, 2004; Lau & Zhou, 2012; Stephens et al., 2018). Trends in extreme rainfall are less subject to energetic constraints (Allen & Ingram, 2002) and often explained in terms of a Clausius-Clapeyron (CC) scaling of 7% increase in the moisture holding capacity of air per degree of surface warming. Sub-CC and super-CC scalings are found in different regions (e.g., Bao et al., 2017; Chou et al., 2013; Singleton & Toumi, 2013), but precipitation increases in the absence of moisture limitations are generally agreed upon (e.g., Fischer & Knutti, 2016; Prein et al., 2016). If these increases are decomposed into those from isolated versus organized convection, the latter is 4 times more likely to produce rainfall intensities of greater than 2 mm/hr (Rossow et al., 2013).

While patterns of cyclone intensification and associated precipitation have been well studied, long-term effects of warming on mesoscale convection are not fully understood. This gap is an important link in a hierarchy of convective scales from individual thunderstorms up to hurricanes. Along with precipitation, convective properties like system depth, width, core-to-core proximity, and speed also adjust to warming (Romps, 2011). Changes to the large-scale circulation have a strong influence on these properties. As the zonal SST gradient drops across the Pacific during El Niño, the overlying pressure gradient and trade winds weaken, and an anomalous easterly flow forms in the West Pacific. Internal dynamics of convective organization also feed back on this large-scale circulation. For example, the upper-level latent heating by convective updrafts enhances atmospheric stability, and the proximity of many updrafts in an organized convective system tends to generate more turbulence and shear (Becker et al., 2018; Romps, 2014). As convection aggregates, the quiescent environment also becomes drier and the quantity of outgoing longwave radiation decreases (Holloway et al., 2017).

Much current understanding of how convection organized on the mesoscale should adjust to surface warming comes from idealized simulations or regionally limited data (e.g., Anderson & Arritt, 2001; Feng et al., 2018; Laurent et al., 2002; Morel & Senesi, 2002; Muller, 2013; Prein et al., 2017). Models are natural tools to predict changes in weather system properties, but the combination of large overall extent and smaller embedded elements makes convective organization particularly challenging to parameterize and forecast. While coupling of precipitation and circulation at the meso-γ and meso-β scale from 2 to 200 km appears to be tightest, it is also the scale least well represented by convective parameterization (Klocke et al., 2017). Even cloud-resolving simulations of mesoscale storms are hampered by their turbulence and microphysics parameterizations, domain-size sensitivity, and imposed large-scale forcing (Hasino et al., 2013). Particularly in the tropics, the majority of simulations with limited domain and prescribed boundary conditions do not include the important interaction of convection with the large-scale circulation (Anber et al., 2015; Kuang, 2007).

As the diversity and resolution of our observations improve, measurement-based studies have also begun to appear. Feng et al. (2016) recently employed a combination of satellite, radar, and rain gauge observations to show that recent changes in the extreme and total rainfall in the central United States are due in large part to MCS that form over the Rockies. Roca et al. (2014) have shown that MCS of 12-hr duration or longer bring 75% of tropical precipitation, and the subset of these systems traveling 250 km or more bring 60%. Several studies have compiled climatologies of tropical rainfall (Elsaesser & Kummerow, 2010; Houze et al., 2007; Zipser et al., 2006), and Henderson et al. (2017) have shown that organized precipitation causes much of the discrepancy between Tropical Rainfall Measuring Mission (TRMM) Microwave Imager (TMI) and precipitation radar (PR) retrievals during El Niño periods. They have also used TRMM data to show an increase in upper tropospheric (UT) moisture and stratiform rainfall during El Niño periods (Henderson et al., 2018). To build upon these efforts, we present tropics-wide, long-term climatologies of the properties of organized convection and its associated rainfall, based upon remote sensing observations and differentiating for El Niño phase.

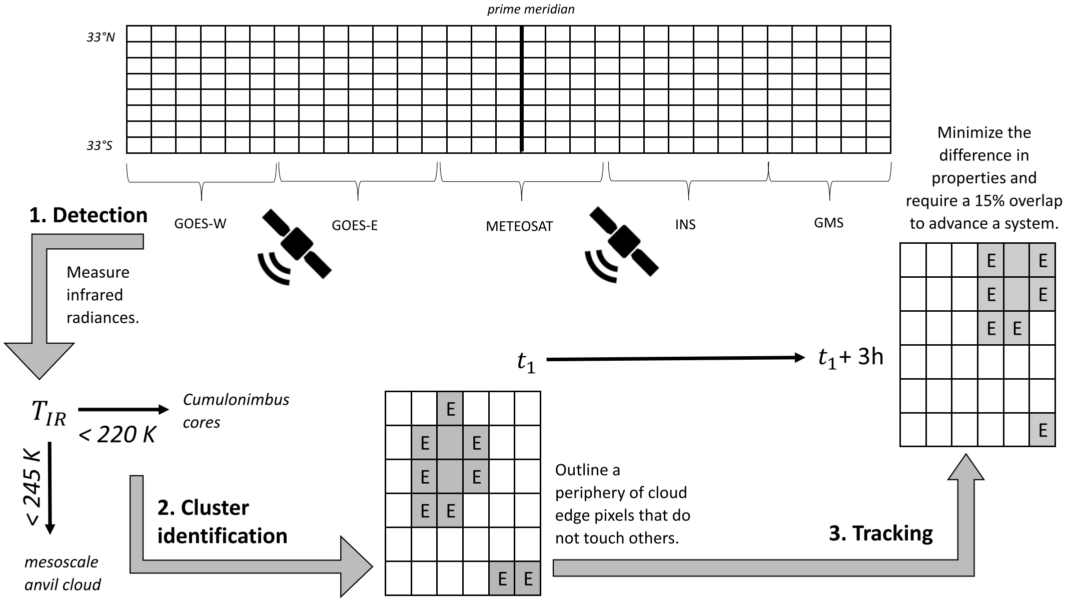

Figure 1. Schematic of the organized convective system (1) detection, (2) cluster identification, and (3) tracking within the International Satellite Cloud Climatology Project DX database.

2. Data and Methods

2.1. Detection and Tracking of Organized Convection

Data on occurrence and properties of deep convection come from the International Satellite Cloud Climatology Project (ISCCP) pixel-level cloud product called the DX data set between July 1983 and July 2008 (Rossow & Schiffer, 1999; Rossow et al., 1996). The ISCCP DX data set is based upon the satellite-measured radiances in the atmospheric window IR band at ≈11 μm and visible band at ≈0.6 μm to distinguish cloudy and clear pixels. Brightness temperature, T_{IR}, is calculated from these radiances, and high-level clouds are identified as those with $T_{\mathrm{IR}} \leq 245$ K (Figure 1). Equating T_{IR} with cloud top temperature implies that the cloud acts as a blackbody to absorb all incident IR radiation, approximately true for very opaque clouds in the IR band where absorption efficiency is close to 1 (Kidder & Haar, 1995). Even for these optically deep clouds, this radiative temperature lies 1 to 2 km below the cloud top (Sherwood et al., 2004).

Thereafter, cloudy pixels are grouped into horizontal clusters (Figure 1(2)). Pixels with one or more edges adjacent to a clear-sky pixel are classified as cloud edge pixels, and a unique cluster has a periphery of cloud edge pixels that do not touch another cluster (Machado & Rossow, 1993; Wielicki & Welch, 1986). This clustering is done both with a T_{IR} threshold of 245 K or less noted above and also with a more stringent value of 220 K or less. This approach was first documented in Machado et al. (1998) and has been widely used and developed since (e.g., Laurent et al., 2002; Masunaga et al., 2005; Morel & Senesi, 2002). The first set of clusters can be understood as mesoscale anvil cloud, and the latter as the cumulonimbus clouds embedded within the larger system. In general, regions of colder T_{IR} are optically thicker. We refer to these classifications as the convective system and core, respectively. The maximum zonal and meridional extent of the cloudy clusters is recorded for each detection in the database.

A variety of T_{IR} thresholds has been used in the past to define cold cloud shields, for example, from 207 up to 253 K in Machado et al. (1992). These showed relative insensitivity of the cluster populations to the threshold, as did tests by Fiolleau and Roca (2013) during their development of the Tracking Of Organized Convection Algorithm through a 3-D segmentatioN (TOOCAN). T_{IR} depends both on cloud top temperature and cloud emissivity/optical depth, so at warmer T_{IR}, midlevel clouds may be spuriously assigned to the anvil. TOOCAN employs a 235-K threshold (Bouniol et al., 2016), as does the recent study of Wall et al. (2018) on anvil lifecycle using Himawari-8 data. Our 245-K threshold may include anvil regions with emissivity down to 0.65, while a value of 235 K allows for clouds with emissivity down to 0.75 (Protopapadaki et al., 2017). Several methods also combine T_{IR} and the extent of a precipitating region (Feng et al., 2016; Yuan

& Houze, 2010). Although we have not used this combined detection, distributions of precipitation accumulation and intensity collocated with the convective systems have modes around 200 m^3/s and 2 mm/hr, respectively, and we have retained only systems with at least one core meeting the 220-K threshold.

From this detection, the location, cloud top temperature, and extent of both systems and cores can be recorded. The extent is calculated as an equivalent radius of the area covered by the pixels; that is, $r = [(n \text{ x } a)/\pi]^{1/2}$, where n is the number of pixels and a is 900 km^2 for pixels with an area of 30 km by 30 km (Machado & Rossow, 1993). An extent criterion of 90 km in equivalent radius, that is, 3 pixels, is enforced. At this spatial resolution, cores must have an equivalent radius of at least 16 km ($\approx [900 \text{ km}^2/\pi]^{1/2}$), so that we do not capture smaller thunderstorm convection; however, we are interested in convective organization on the larger meso-α scales in any case. If the meso-β and meso-α scales are divided at the 200-km length scale, 75% of our features are meso-α at any given time and 95% reach meso-α at some point in their lifetime. A total of 1,647,238 such features with embedded cores is detected with an average system equivalent radius of 133 km. They have on average 2.9 embedded convective cores with an average equivalent radius of 25 km.

The 3-hourly temporal resolution of the satellite measurements should capture all occurrences of longer-lived convective organization. The threshold to qualify as a convective system is generally set at 4 hr or longer (Bouniol et al., 2016; Hagos et al., 2013; Tsakraklides & Evans, 2003). Three-hourly resolution has also been used in other studies to identify the influence of vertical wind shear, convective available potential energy (CAPE), and aerosol concentrations on convective lifetimes (Chakraborty et al., 2016); to evaluate expected duration and diurnal variation in deep convective events (Ricciardulli & Sardeshmukh, 2002); and to develop life cycle statistics for both continental and oceanic systems (Mapes et al., 2009; Vant-Hull et al., 2016). The life cycle of these systems is generally understood in three phases—deep convective initiation, surrounding stratiform development, and system dissipation (Bouniol et al., 2016; Houze, 2004)—and system duration can range from 9 or 10 hr up to 30, dependent on both the dynamic and microphysical conditions (Feng et al., 2018; Punkka & Bister, 2015). More recent regional convective databases are moving toward hourly or even half-hourly temporal resolution to better illustrate this evolution (Feng et al., 2016; Roca et al., 2017). Although higher resolution is desirable, the advantage of our data is its long duration and consistent coverage, which allow us to build robust ENSO-related signals.

The tracking aspect of the database constructs a 5° × 5° box (assuming here that the system velocity is less than 60 m/s) around each system center and queries this box in the subsequent +3-hr satellite image for the continued presence of systems (Figure 1(3); Machado et al., 1998). A 15% areal overlap requirement is also imposed. This area-overlapping technique has historically been the most commonly used with threshold values from 5% to 50% (Arnaud et al., 1992; Fiolleau & Roca, 2013; Goyens et al., 2011). Some studies have also used fractional overlap as a function of system size (Williams & Houze, 1987). Machado et al. (1998), with the same methodology as this study, found limited sensitivity of convective properties to their tracking parameters. If a proceeding system is found, a weighted average between all of its properties and all of those of the preceding system is calculated. If there are other candidate preceding systems, an average is calculated for each, and the system is assigned to the preceding system with the most similar properties. If no match is made, the track ends. A subtlety of this process is the possibility for system splitting and merging. For splitting, the database will record the more similar of the two systems to the preceding one and initiate the second as a new system. Merges far outnumber splits (Vant-Hull et al., 2016), and the database terminates the track of a smaller system that has merged with a larger one. Alternative methods could continue to classify both split elements of a system as the initiating system or to classify a merged system as a new one, rather than a continuation of the initiating one (Machado et al., 1998; Williams & Houze, 1987). Relative to the techniques employed here, the first of these should identify less frequent, longer-lived systems, while the latter should identify more frequent, shorter-lived systems.

2.2. Collocated Meteorology and Precipitation

With this convective tracking database, we collocate SSTs and CAPE from the European Centre for Medium-Range Weather Forecasts interim reanalysis (ERA-Interim) at 1° and 6-hourly resolution (Dee et al., 2011). If there is no exact temporal collocation, we take the value preceding system passage by 3 hr. Spatial collocation is done to the nearest full degree latitude and longitude from the system center or the system core. Local SST anomalies are calculated below as the difference in the local SST and the December–February climaotological mean between July 1983 and July 2008.

Precipitation data come from the Multi-Source Weighted-Ensemble Precipitation (MSWEP) project version 2.2 at 0.5° spatial and 3-hourly temporal resolution over the same time period (Beck et al., 2017). MSWEP synthesizes rain gauge (Climate Prediction Center Gauge-Based Analysis of Global Daily Precipitation and the Global Precipitation Climatology Centre) and satellite measurements (CPC morphing, Global Satellite Mapping of Precipitation, and Tropical Rainfall Measuring Mission Multisatellite Precipitation Analysis) with reanalysis data (ERA-Interim and the Japanese 55-year Reanalysis). These products were selected based on the accuracy of their temporal variability relative to a bias-corrected long-term mean from the Climate Hazards Group Precipitation Climatology (Funk et al., 2015).

The chosen satellite and reanalysis products are merged with rain gauge measurements, where the latter are weighted according to gauge density at a given location and the former according to their agreement with the nearest rain gauges. The advantage of this methodology is that a synthesis of products overcomes the biases in each individually. For example, elevation biases and wind-induced undercatch exist for purely gauge-based data sets, and given the highly localized nature of precipitation, their utility is in proportion to their density (Kidd et al., 2017). Satellites obviate the issue of coverage for gauges, but at the expense of seasonal biases related to snow and ice cover and insensitivity to light rainfall (Kidd et al., 2012). Reanalysis captures the precipitation associated with synoptic systems well but may fail for more sporadic convection (Beck et al., 2017). Given that annual precipitation may vary by up to 300 mm from one data set to the next (Sun et al., 2017), a combination of data types is a promising approach, similar to the utility of climate model ensembles relative to a single model run. Indeed, in an intercomparison of long-duration gauge-corrected precipitation products, MSWEP data produced the highest temporal correlation coefficients with pure gauge measurements (Beck et al., 2017).

From the MSWEP V2.2 values, we calculate precipitation accumulation by summing precipitation rate from the minimum latitude and longitude up to the maximum latitude and longitude covered by the convective system and assuming that each 0.5° × 0.5° grid cell has an approximate area of 3,025 km^2. The maximum precipitation intensity is the single highest value within the subdomain over which the precipitation accumulation is calculated.

2.3. Collocated High-Cloud Properties

As the deep convective cloud systems determined by ISCCP only include the thicker part of the anvils with a T_{IR} threshold of 245-K and IR emissivity threshold of about 0.6 (Figure 2 of Protopapadaki et al., 2017), we also collocate these convective systems with UT cloud systems, identified from IR sounder retrievals of cloud top pressure p_{cld} and emissivity ϵ_{cld} (Stubenrauch et al., 2013). The high spectral resolution of these instruments allows reliable cirrus identification, down to an IR optical depth of 0.1, both during daytime and nighttime (Stubenrauch et al., 2013). Since 2002, aboard the Aqua satellite, the Atmospheric Infrared Sounder passes the tropics at 01:30 and 13:30 LT, providing bidaily data with a spatial resolution of 13.5 km at nadir (Chahine et al., 2006). High-level clouds are defined by $p_{\mathrm{cld}} \leq 440$ hPa, and UT cloud systems are constructed by merging adjacent grid cells of 0.5° latitude by 0.5° longitude with similar p_{cld} ($\Delta p_{\mathrm{cld}} < 50$ hPa). Convective cores, cirrus anvil, and thin cirrus within these systems are then identified by $\epsilon_{\mathrm{cld}} > 0.98$, $0.98 > \epsilon_{\mathrm{cld}} > 0.5$, and $0.5 > \epsilon_{\mathrm{cld}} > 0.1$, respectively (Protopapadaki et al., 2017). These data are referred to as the upper tropospheric cloud system (UTCS) database hereafter.

2.4. El Niño Indices

A variety of indices exist to differentiate the warm and cold phases of ENSO. The Oceanic Niño Index (ONI), which we use here, is the most commonly used. ONI is defined as the SST anomaly (SSTa) in the Niño 3.4 region from 5°N to 5°S and from 120°W to 170°W using the National Oceanic and Atmospheric Administration/National Climatic Data Center Extended Reconstructed Sea Surface Temperature data set version 5. Given recent warming trends, anomalies are now calculated from a 30-year base period. So, for example, ONI values for 1990 will be calculated from the mean of a 1975-to-2005 base period. To classify as an El Niño month, the ONI must be greater than +0.5 in a 3-month running mean. Likewise, to be classified as a La Niña month, the mean ONI must be less than −0.5 for a 3-month span. “El Niño climatologies” or “El Niño means/statistics” then refer to the convective data and/or its collocated meteorology and precipitation during all months classified as El Niño. ONI values are available online (www.esrl.noaa.gov/psd/data/correlation/oni.data).

The Multivariate ENSO Index (MEI) will also be used below and is calculated as the first empirical orthogonal function of a combination of sea level pressure, zonal and meridional surface winds, SST, and outgoing

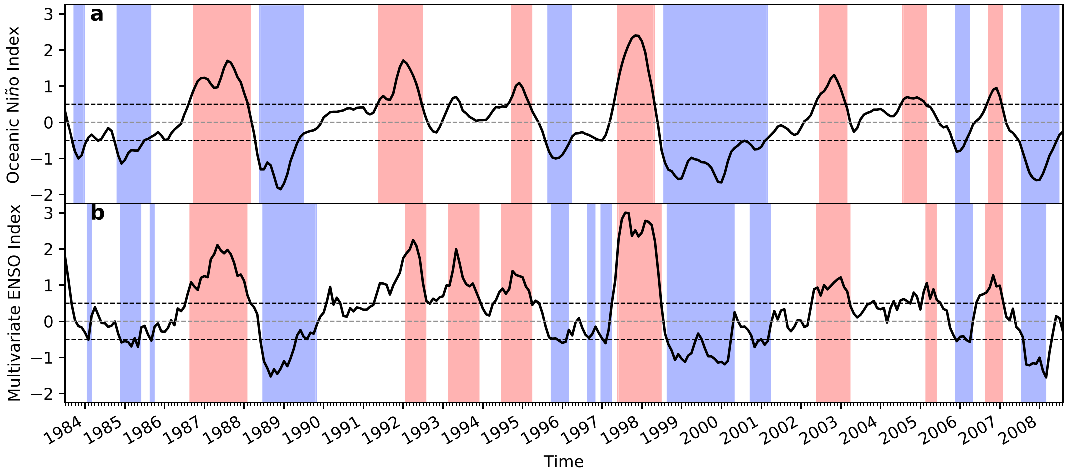

Figure 2. Oceanic Niño Index (a) and the Multivariate ENSO Index (b) over the period of interest from July 1983 to July 2008. El Niño and La Niña periods are highlighted in red and blue respectively, and values of 0 and ±0.5 are shown in dashed lines. ENSO = El Niño–Southern Oscillation.

longwave radiation over the Pacific from 30°S to 30°N and from 100°E to 70°W. These empirical orthogonal functions are calculated with a 2-month running mean, and their values are available online (www.esrl.noaa.gov/psd/enso/mei/). Time series of both the ONI and MEI for the duration of the ISCCP convective tracking data are shown in Figure 2. The two metrics allow us to see the impact of El Niño in different ways. With its incorporation of data on the atmospheric state, the MEI yields convective trends of larger magnitude. By requiring the synchronization of more environmental variables, MEI is also less likely to pick up on transient El Niños than is the ONI. Transient El Niños refer to periods in which the atmosphere-ocean feedbacks have not yet stabilized. For example, westerly wind bursts generally precede eastern Pacific warming, but this warming does not necessarily feedback on wind or convective anomalies (Hameed et al., 2018). MEI will tend to exclude periods like these, while ONI on the basis of SST alone will tend to include them, generating smoother classifications with longer autocorrelation time scales.

Other indices may use a longer running average (Niño 3.4 Index), temperature gradients over a wider equatorial span (Trans-Niño Index), air pressure anomalies rather than SSTa (Southern Oscillation Index), or a Niño-3.4 region anomaly relative to the global mean SST (Cold Tongue Index). In general, correlation coefficients between any of these indices are at least 0.75 or higher (Wolter & Timlin, 2011, their Table 1). In all analyses, the tropics are defined as longitudes and latitudes between 33°S and 33°N, a domain about 10° outside of the Tropics of Cancer and Capricorn that allows us to see both tropical and subtropical effects.

3. Changes in the Occurrence and Structure of Organized Convection

We begin by examinining differences in the occurrence and horizontal and vertical extent of organized convective systems, differentiated by season and ENSO phase. These difference climatologies reflect the atmospheric impact of oceanic warming on the zonal overturning (Figures 3a–3d). The relative differences are shown, meaning that a value of +10% can be interpreted as a 10% gain in a value during El Niño periods relative to La Niña ones. To test the robustness of these results, we use the two different ENSO metrics described above.

3.1. Occurrence

The occurrence of organized convection over the central and East Pacific increases during El Niño (Figure 3a) based upon ONI, reflecting the eastward migration of the ascending branch of the Walker circulation during the warm phase. Occurrence of organized convection increases by as much as a factor of 3 in regions of highest positive SSTa (Figure S1 in the supporting information). Outside of the warmer Niño 3 and 4 regions, convective systems are up to 2 times less frequent during El Niño. Over the Maritime Continent and Amazon, where regions of ascent intensify during La Niña, system occurrence increases by about 50% locally in the cold phase.

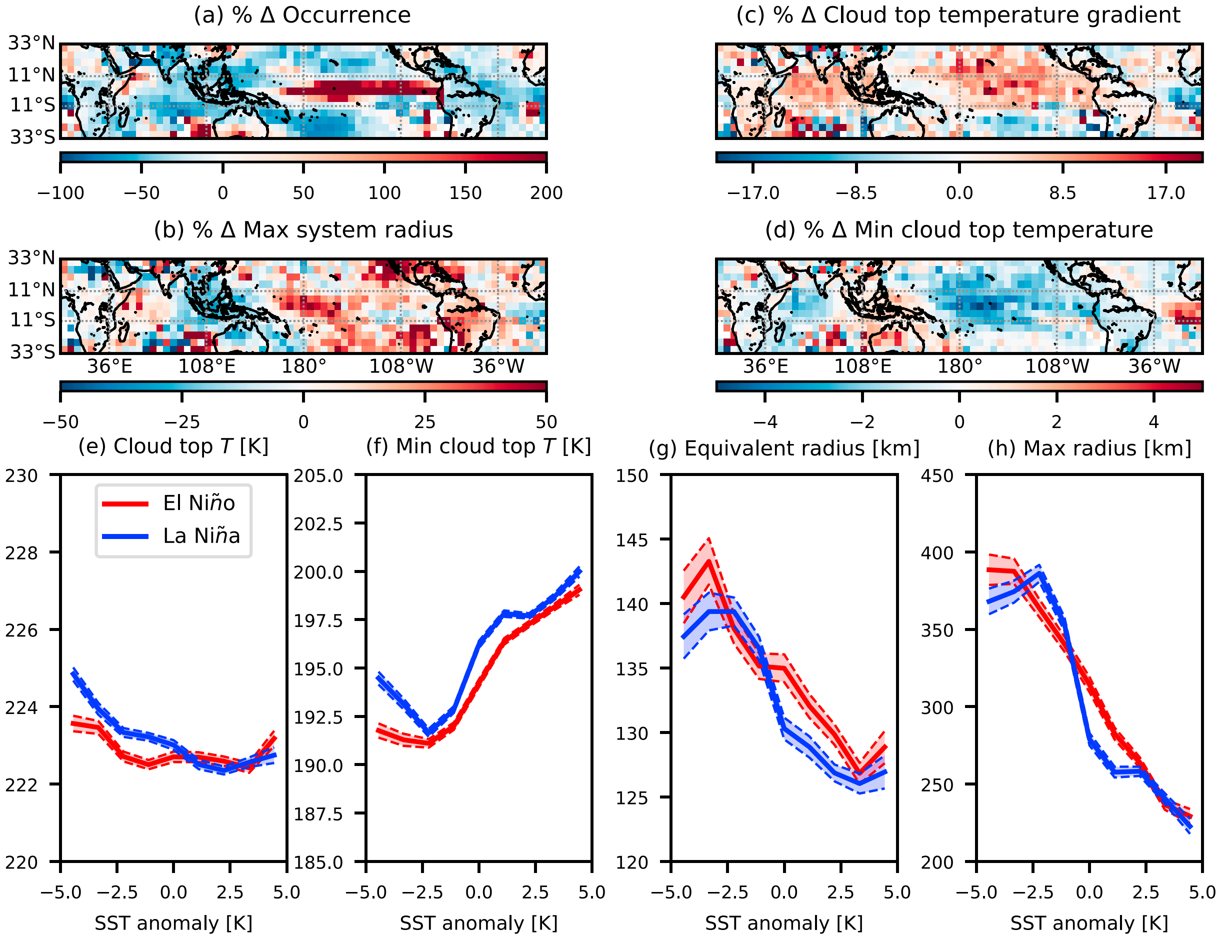

Figure 3. Climatologies of the relative differences between El Niño and La Niña (for which Oceanic Niño Index $\gtrless \pm 0.5$, respectively, between July 1983 and July 2008) in occurrence, horizontal extent, cloud top temperature gradient (maximum minus minimum cloud top temperature divided by their separation distance), and minimum cloud top temperature of convective organization (panels a to d). All fields are coarse grained to a 5° grid, shown for boreal winter (December–February), and normalized by the La Niña value. A relative difference of +10% represents a 10% increase in the value during El Niño relative to La Niña at that particular grid cell. Relative increases during El Niño are shown in red, but note that an increased cloud top temperature implies a shallower system. Binning of local temporal sea surface temperature (SST) anomaly versus instantaneous cloud top temperature T_{top} (e), minimum T_{top} (f), instantaneous equivalent radius r_{eq} (g), and maximum r_{eq} (h). The mean is shown in a solid line with a 95% confidence interval for its value filled between the two dashed lines for both El Niño and La Niña.

Redistribution of convective activity can be understood in terms of the dominant tropical balance of heating and vertical advection. Because the tropical atmosphere does not sustain large horizontal tropospheric temperature gradients, as the surface warms, convective activity shifts to these warmest SST regions and shuts down over the cooler ones (Sobel, 2010). The saturation water vapor mixing ratio, $q_{v,\mathrm{sat}}$, also increases with warming temperatures according to the CC relationship, allowing larger saturation deficits ($q_v - q_{v,\mathrm{sat}}$) to build up. In regions where saturation deficit increases, so does the CAPE, meaning that there is more energy available to air parcels to ascend convectively. A recent modeling study illustrates how CAPE extremes increase in a warming climate (Singh et al., 2017), and we see similar shifts in the 99th percentile of the distributions of CAPE extremes during El Niño relative to La Niña (Figures S4c and S4d).

Using the MEI rather than the ONI, the climatology of occurrence differences is the same qualitatively, but with quantitatively larger trends, particularly in the occurrence decreases outside of the equatorial Pacific. The atmospheric signal is stronger with MEI because it incorporates sea level pressure and outgoing longwave radiation values, along with SST. A greater duration of time is classified as El Niño with MEI relative to ONI (Figure 2), and MEI is less likely to record transient periods in which ocean-atmosphere feedbacks are not well established. Both of these distinctions amplify its warm phase signal.

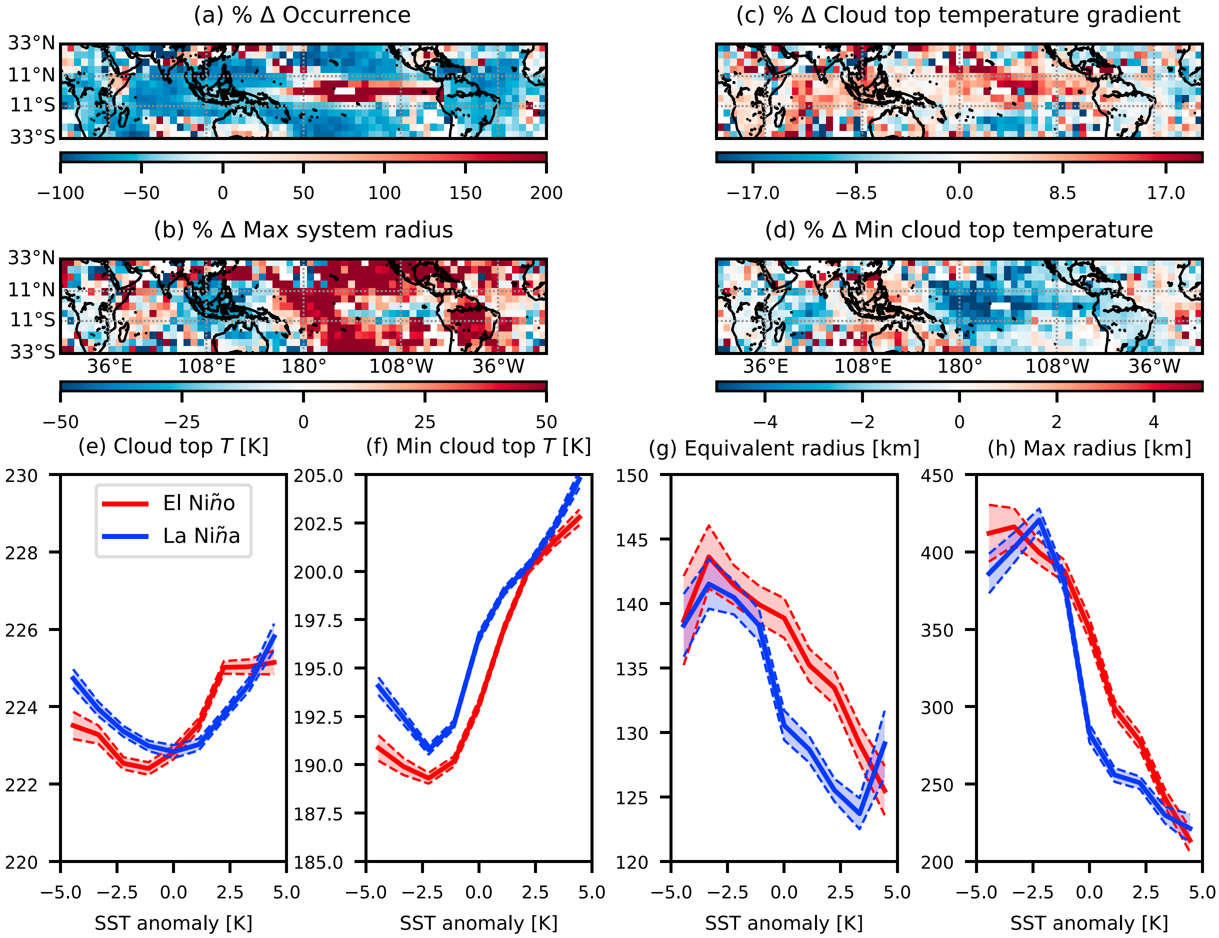

Figure 4. Climatologies of relative differences in convective properties between El Niño and La Niña (for which multivariate El Niño–Southern Oscillation index is greater than its 80th percentile or less than its 20th percentile, respectively between July 1983 and July 2008) (panels a to d), as in Figure 3. Binning of local temporal sea surface temperature (SST) anomaly and convective properties (panels e to h), also as in Figure 3.

Finally, we can consider the tropics-wide SSTa dependence of the organized convective occurrence over time, given the long duration of our data set. In regressions of tropics-wide monthly averaged SSTa and tropics-wide monthly averaged convective occurrence during El Niño periods in the 1980s, 1990s, and 2000s (Figure S2), the SSTa dependence of occurrence weakens during the most recent and warmest decade. We can summarize by saying that El Niño sea surface warming coincides with a localized increase in convective system frequency by as much as a factor of 3, a trend whose magnitude amplified when classifying by MEI and whose SSTa dependence weakens in recent decades. These shifts in occurrence of organized convection can be understood in terms of tropical weak temperature gradients and increases to CAPE extremes during El Niño.

3.2. Horizontal Extent

We next investigate horizontal extent and its lifecycle maximum, corresponding to the mature stage of convection. Along with greater occurrence, organized convection tends to have a greater maximum coverage during El Niño (Figure 3b). The largest increases occur in the Niño 4 region and off the western coasts of North and South America, where systems can be up to 50% greater in El Niño relative to La Niña, meaning for example a 150-km gain in equivalent radius during El Niño for a 300-km system. Off the coast of California and Mexico in the Northern Hemisphere, atmospheric rivers could play a role, as these jets of water vapor transport have been observed to intensify during El Niño periods (Kim et al., 2017). Off the coast of Peru and Chile, a small increase in the typically cool SSTs may be enough to allow the extensive stratocumulus decks there to deepen and then spread. The relative increases amplify when using MEI to differentiate El Niño and La Niña (Figure 4b). As above, trend amplification may be due both to the addition of atmospheric information and omission of transient periods in which ocean-atmosphere feedbacks are weaker.

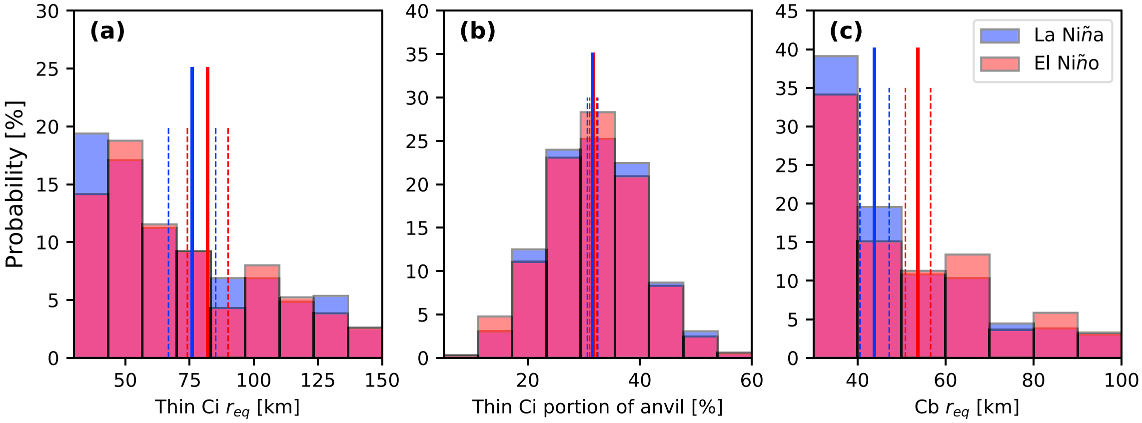

Figure 5. Probability distributions of the thin cirrus (a), thin cirrus fraction of the anvil (b), and cumulonimbus (c) coverage from the upper tropospheric cloud system database in percentage collocated with systems from the International Satellite Cloud Climatology Project CT database between 2003 and 2008. Those from El Niño are shown in red, and those from La Niña are shown in blue. The mean of the distributions is shown in a solid line with a 95% confidence interval given in dashed lines.

The use of the full Pacific basin SST in MEI, rather than only that of the Niño 3.4 region, should also make this metric more sensitive to the central Pacific El Niños that have been recently increasing in frequency.

If we consider average horizontal extent of these systems, rather than the maximum over their lifetime, the increase over the central Pacific drops from 50% to about 12%. In decomposing these trends by lifetime ($t \leq 3$ hr, 6 hr $\geq t > 3$ hr, and $t > 9$ hr), the climatological change in maximum coverage is driven by the longest-lived systems and that in average coverage by the short-lived ones (Figure S5). This is expected as the primary means of system expansion is through growth of the stratiform region with the decay of convective cores (Houze, 2004).

What is the relationship between local SSTa and this expansion of convective systems during El Niño? In panels (g) and (h) of Figures 3 and 4, we show mean horizontal extent and its lifetime maximum as a function of SSTa, binned to 10 values between −5 and +5 K, separately for El Niño and La Niña months. These local values are taken from the 1° grid prior to coarse graining, and the 95% confidence interval for the mean convective property is also shown in dashed lines. SSTa are calculated as the temporal difference of the ERA-Interim SST (at 3-hourly resolution) collocated to the ISCCP systems from the December–February SST climatology between 1983 and 2008. For both ENSO metrics, extent and its lifetime maximum decrease as the SSTa increases, but with larger slope or sensitivity during La Niña. The largest discrepancy in dependencies between the two ENSO phases occurs at warm SSTa up to +2 K and when classifying by MEI.

The radiative impacts of this expansion outside of the warm SST regions will differ, depending on the part of the system from which these changes come from: Thin upper-level cirrus tend to warm the upper atmosphere, while the optically thick cores cool. To decompose these changes, we show probability distributions of different system components from the UTCS database in Figure 5. The UTCS and ISCCP data overlap for only 5 years between 2003 and 2008, during which ENSO activity is limited (i.e., $|\mathrm{ONI}| < \pm 1$), reducing the statistics. The distribution of total size from the convective tracking contains more instances of small systems, while that of UTCS is more skewed with a few more instances of very large systems (Figure S3). For this reason, we enforce an asymmetric filter of [−50 km, +100 km] for the UTCS-ISCCP difference in Figure 5. With this filtering, associated cumulonimbus clouds are more extensive during El Niño by 10 km in r_{eq} at 95% confidence. Thin cirrus coverage is slightly larger during El Niño as well, although the El Niño-La Niña difference in means is only significant at the 65% level (Figure 5a). The thin cirrus portion of the anvil does not show clear trends.

Different hypotheses to explain potential reductions in upper-level cloud with warming have been put forward, as such a mechanism would constitute a negative feedback. Increased convective aggregation (Mauritsen & Stevens, 2015), higher precipitation efficiency (Lindzen et al., 2001), or a microphysical shift toward faster-sedimenting graupel from snow (Tompkins & Craig, 1999) may all lead to reductions in upper-level cloud and apply both to the anvil outflow of convective systems and to isolated cirrus. More recently, Bony et al. (2017) proposed that increased upper atmospheric stability with surface warming weakens cirrus detrainment. Their focus was on the anvil outflow component of upper-level cloud change (also the only component addressed here) and employed uniform surface heating in idealized simulations. For, instead, a changing Pacific SST gradient during El Niño in our ISCCP observations, we also see smaller systems forming over warmer local SSTa (Figures 3g and 3h). Quantitatively, r_{eq} drops by about 15 km/K, or 1%/K for a 150-km radius system, similar to values from the Institut Pierre-Simon Laplace model between 1979 and 2005 (Bony et al., 2017). Along with this 15-km/K scaling, we have found relative increases in the maximum horizontal extent of systems up to 50% in the central Pacific and off the coasts of the Americas, with the largest contributions from the longest-lived systems and their cumulonimbus portion. Classification by MEI amplifies these El Niño-La Niña extent differences by up to a factor of 2.

3.3. Vertical Depth

Lastly, we consider climatologies of the vertical depth of organized convection, quantified by cloud top temperatures (T_{top}) and T_{top} vertical gradients (defined as the maximum minus minimum cloud top temperature divided by their separation distance, Figures 3c and 3d). Both T_{top} and its gradient tend to be colder during El Niño, meaning that systems deepen both on average and relative to their horizontal extent. This result can be separately reproduced using solely UTCS data (not shown). The deepening of convective organization is most prominent in the central Pacific, the region to which the ascending branch of the Walker circulation has shifted eastward. Convective divergence does not balance clear-sky convergence in the presence of this large-scale ascent, and convection can deepen further here. This finding is in agreement with other studies of colder cloud top temperatures associated with deep convection during the ENSO warm phase (Li et al., 2012; Masunaga et al., 2005). Anomalies in convective depth are also more meridionally diffuse than those in convective occurrence or extent, most likely because these deepest convective towers generate gravity waves that propagate anomalies outward (Chiang & Sobel, 2002).

How does this deepening relate to the hypotheses of fixed-anvil temperature (FAT) and proportionately higher anvil temperature? FAT refers to the idea that convective anvils form at the altitude where clear-sky radiative cooling drop off and convective detrainment into these regions maximizes (Hartmann & Larson, 2002). Because the radiative cooling is determined by the vertical gradient of water vapor specific humidity, the temperature at this altitude should be fixed and independent of surface warming. Proportionately higher anvil temperature then refers to adjustments in this otherwise fixed altitude as static stability changes with warming (Zelinka & Hartmann, 2010). More recently, Seeley et al. (2019) have examined these theories and stated that the more accurate term is a fixed tropopause temperature: Anvil temperatures can vary by up to 40% of the surface temperature range, while the radiatively defined tropopause varies by less than 4%. With ONI classification, instantaneous cloud top temperatures show limited dependence on local SSTa. Looking at Figure 3e, the range of 2-K difference in average T_{top} for a 10-K range in SSTa is of the same order as the 23% change in anvil temperature reported for full-complexity radiative-convective equilibrium simulations (Seeley et al., 2019). $\partial T_{\mathrm{top}}/\partial \mathrm{SSTa}$ is lower for El Niño than La Niña also in agreement with radiative-convective equilibrium simulations for which ΔT_{top} gets smaller at warmer surface temperatures, although the cause of this reduction is not yet understood (Seeley et al., 2019, their Figure 4).

Now, if we classify instead by MEI (Figures 4g and 4h), we see somewhat stronger SSTa dependence of T_{top}. This breakdown in the FAT can be attributed to the violation of clear-sky convergence balancing convective divergence. Periods of high-magnitude MEI imply that the zonal overturning has had time to stabilize relative to surface warming. An established zonal overturning generates regions of large-scale ascent and descent where clear-sky convergence no longer equates to convective divergence. Indeed, in the difference climatologies, the regions where convection deepens most are those most strongly affected by the large-scale Walker-cell ascent. We can better see this impact of circulation on $\partial T_{\mathrm{top}}/\partial \mathrm{SSTa}$ by stratifying the SSTa dependence of T_{top} into central and West Pacific and Atlantic subdomains (Figure S6). The strongest signals of $\partial T_{\mathrm{top}}/\partial \mathrm{SSTa}$ occur over the central Pacific. In this region, large-scale descent occurs during La Niña within the Walker circulation, warming cloud top temperatures, while large-scale ascent occurs during El Niño, deepening systems to colder cloud top temperatures.

Within this discussion, it is important to keep in mind the difference between satellite-measured T_{top} and the maximum detrainment level (Li et al., 2012). While detrainment may be maximized at the tops of isolated shallow cumulus and cumulonimbus, the two are not necessarily the same within convective systems (Johnson et al., 1999). In Figure S4e, divergence profiles from reanalysis collocated with organized convection are shown during both El Niño and La Niña. The magnitude of mean divergence is less during El Niño above about 7 km by a factor of 2. But the divergence peaks for both phases at the same altitude of 14 km, approximately validating the idea that peak detrainment levels correspond between phases.

Finally, we consider the opposite responses of convection over the Maritime Continent and the Amazon. Cold SSTa occur adjacent to the extensive coastlines of the Maritime Continent islands during El Niño (Figure S1). Although these increase the low-level pressure gradient and moisture advection (Park & Chiang, 2010), warm phase convective organization is still less extensive and shallower there, given the initial moisture limitation above land and colder waters. SSTa along the South American coasts are also negative, but vegetation can generate surface heat and moisture fluxes that sustain convective systems. Atlantic SST cooling also strengthens low-level baroclinicity and the southern low-level jet centered around 18°S and 62°W (Stensrud, 1996; Vernekar et al., 2003) that initiates deep convective systems, particularly squall lines, that propagate further (Alcantara et al., 2011). Overall, we have shown convective system deepening of up to 5% in regions of large-scale ascent, anomalies that may be propagated meridionally by gravity waves or modulated by land-sea differences. Observed relations are generally in line with the FAT hypothesis: SSTa dependency of T_{top} is weak with the exception of the central Pacific (where the zonal overturning shifts dramatically), and changes to the altitude of peak divergence are small between El Niño and La Niña.

4. Organization Metrics

4.1. Information Entropy for Organization

We now reillustrate the findings from the climatologies above in different forms using two new metrics. First, to more rigorously quantify organization, we calculate the *information entropy* of the monthly average maps of convective occurrence. Information entropy can be understood as the degree of disorder based on probability distributions: As organization increases, entropy decreases. Our algorithm to calculate the information entropy, H, of a cloud field scans for a range of different “feature sizes” from a few grid cells to the entire tropical domain. At each feature size, we calculate the probability that other values in the subdomain agree with that in the upper left corner. The results that follow are not very sensitive to the grid cell used as a reference; that is, the findings are qualitatively the same with probabilities calculated relative to the value in the lower right corner of the subdomain. From these probabilities, information entropy is calculated as follows:

$$H = -\sum_{i=0}^{i=\mathcal{L}^2} p_i \log_2(p_i). \tag{1}$$

H can be between 0 and 0.5, after normalizing by subdomain size. Zero indicates the limit of perfect homogeneity of the subdomain (or equivalently low information content), and 0.5 indicates the limit of perfect heterogeneity (or equivalently high information content). The use of different scanning subdomains $\mathcal{L}^2$ also provides an estimate of the length scale $\mathcal{L}$ for which the entropy is largest and smallest. In other words, is there a certain spatial scale at which convection is most organized? We investigate this question in more detail in future work, but for now, we present H distributions for convective occurrence during El Niño and La Niña months between 1983 and 2008 in Figure 6. Distributions are shown for a variety of feature sizes from two grid cells up to 50.

For all subdomain sizes, the distributions show lower information entropy of the cloud field, that is, more aggregation across scales, during El Niño periods. The means of the cold phase distributions are larger than those of the warm phase distributions with 95% confidence for all window sizes, indicating a general shift toward more organized convective fields during El Niño: Clear regions are more likely to be surrounded by more clear sky, and cloudy regions by more cloud in El Niño relative to La Niña. Stated in terms of information theory, a given cloud field during the warm phase has lower information content because the subdomains over which H is calculated are more homogeneous. The degree of aggregation in the cloud fields increases with subdomain as well. For $\mathcal{L}$ of 2 grid cells (≈220 km), the cold-warm phase difference in median H is 0.034, while for $\mathcal{L}$ of 30 grid cells (≈3,300 km), the difference has increased to 0.055. In between these subdomain sizes, $H_{\mathrm{LN}} - H_{\mathrm{EN}}$ increases monotonically; the more of the cloud field we consider at a time, the larger the increase in its organization during El Niño relative to La Niña. This result corroborates the climatological increases in occurrence, extent, and depth across the tropics and is conceptually similar to El Niño increases in the “cloud correlation-scale length” that represent the probability of finding more cloud adjacent to a cloudy region (Masunaga et al., 2005).

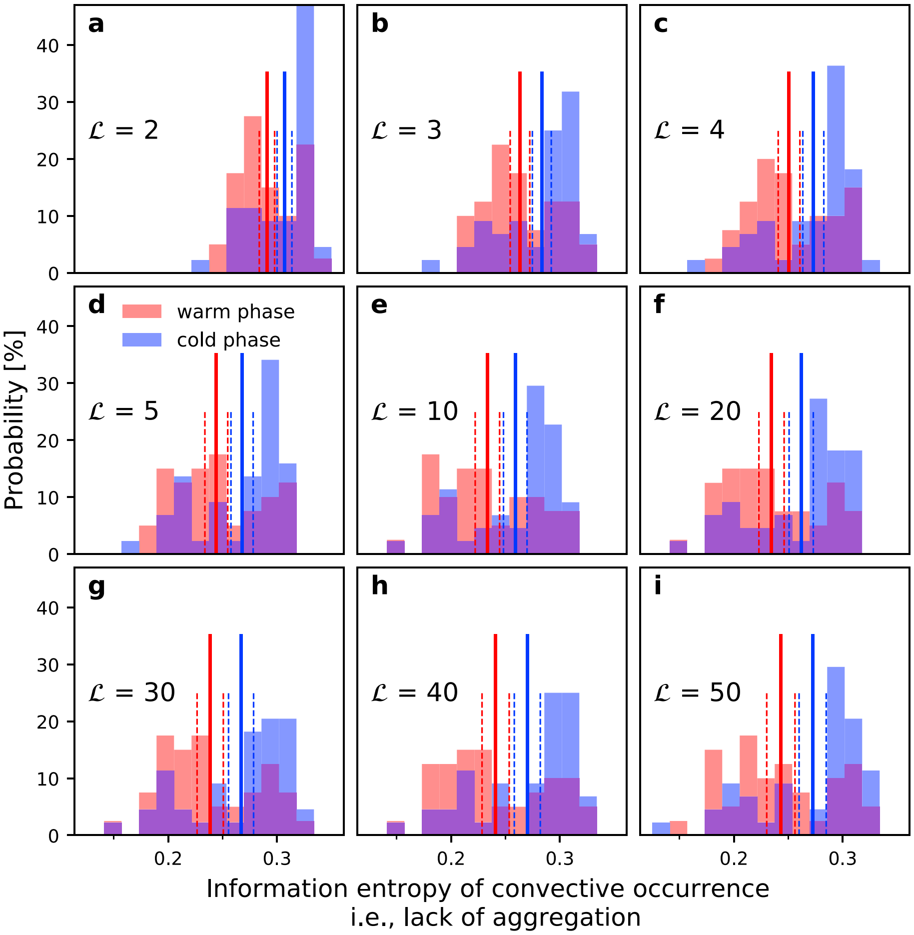

Figure 6. Probability distributions of the entropy metric H of the mesoscale convective occurrence during El Niño and La Niña classified by Oceanic Niño Index, in red and blue, respectively, and for various subdomain sizes from $\mathcal{L}^2$ = 2-by-2 grid cells up to 50-by-50. The means of each distribution are shown in solid red and blue, and the 95% confidence interval shown in dashed red and blue. Lower values indicate a more organized field.

4.2. Growth Metric

The convective tracking data allow us to look at convective structure over time. In particular, a *convective growth metric* can be defined to quantify system deepening relative to spreading (Table S1) or equivalently vertical relative to horizontal growth:

$$\gamma = \frac{\overline{T_{\text{top}}}(t > \tau) - \overline{T_{\text{top}}}(t \le \tau)}{\Gamma\left[\overline{r_{\text{eq}}}(t > \tau) - \overline{r_{\text{eq}}}(t \le \tau)\right]}, \tag{2}$$

where Γ is an assumed lapse rate, T_{top} is cloud top temperature, r_{eq} is the horizontal extent, and t is the system lifetime, differentiating for young ($t \le \tau$) versus mature ($t > \tau$) systems. These values are calculated climatologically from the entire database, rather than for each system individually. In other words, we take the average cloud top temperature and equivalent radius for all systems of greater than τ duration and compare these values with those from systems of less than or equal to τ duration. The negative values of γ that dominate the field in Figure 7 indicate that organized convection is deepening and spreading over its lifetime, while a magnitude on the order of 0.001 indicates that these systems vertically deepen by about 1 K for every 150-km radial expansion, or equivalently that spreading is 1,000 times faster than deepening. The difference in the metric from East to West Pacific indicates different "modes of growth": Moving from a γ of −0.014 in the east to a γ of −0.004 in the west reflects that systems deepen 100 times faster over the positive SSTa off the coast of South America. During boreal winter, the tropics-wide mean γ decreases in magnitude by 18% during El Niño relative to La Niña from a mean of −0.0112 down to −0.0094 for a τ of 3 hr. Figures 7d

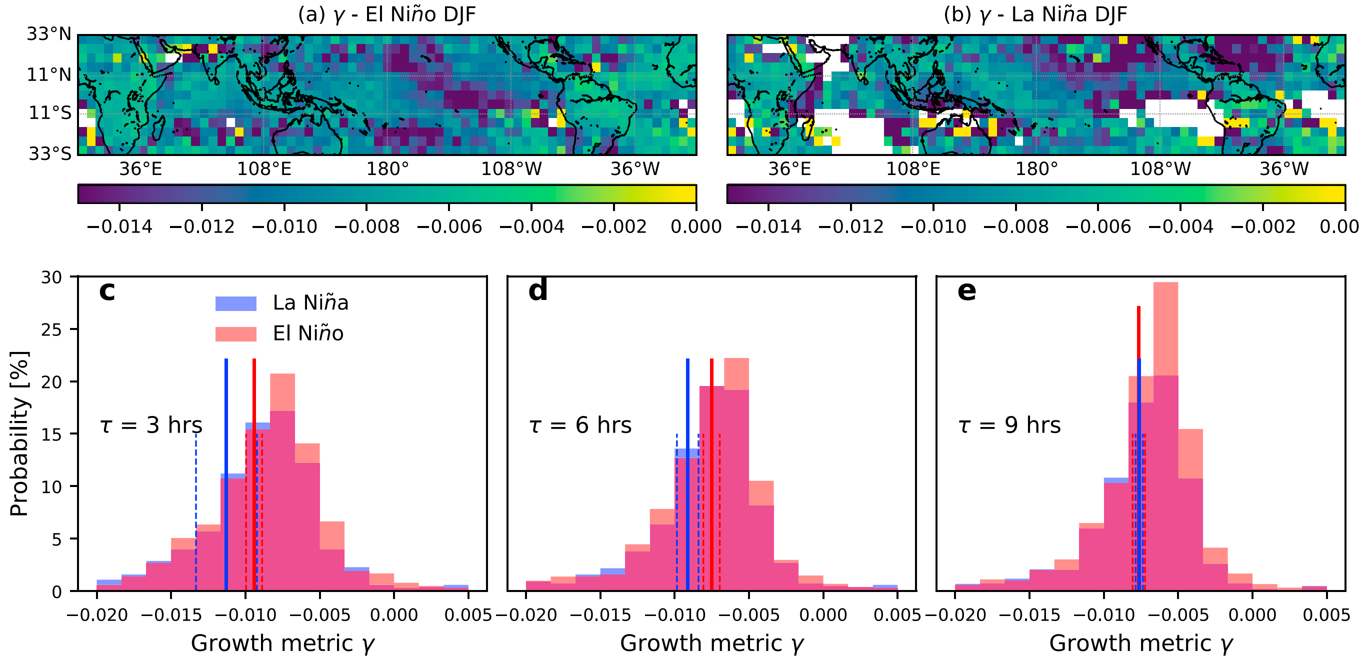

Figure 7. Maps of the organized convection growth metric γ during El Niño (a) and La Niña (b) boreal winter, as classified by multivariate El Niño–Southern Oscillation index. White indicates regions where γ is undefined because of very small changes in r_{eq}. The effect of changing τ is shown with probability distributions of γ in panels (c) to (e). The El Niño and La Niña means are shown in solid red and blue, respectively, with 95% confidence intervals in dashed lines. DJF = December–February.

and 7e show the adjustment of this mean and associated distribution with τ. For a τ of 6 hr, the El Niño mean remains 17.5% below that of La Niña, while for a τ of 9 hr, the discrepancy has disappeared. As τ increases from 3 to 6 to 9 hr, the mean γ value decreases monotonically in magnitude for both phases, indicating the shift from vertical deepening to stratiform broadening over system lifetime.

The growth metric γ provides a nice way to condense structural data over time from the convective tracking information and indicates that while systems during La Niña deepen and decay rapidly, those during El Niño deepen more gradually and accumulate a larger, surrounding stratiform region. We can see a similar trend of more rapid deepening during La Niña, when we analyze life cycle on a per-system basis in Figure 8. Convective tracks are compiled for January 1998 (El Niño: ONI = +2.2, MEI = +2.2) and January 2000 (La Niña: ONI = −1.7, MEI = −1.3), and the duration, extent, and depth are all normalized to their maximum so that values exist between 0% and 100%. El Niño (La Niña) systems have a horizontal growth rate of 52.8% (58.0%) and a vertical growth rate of 33.6% (29.1%) in the first 25% of their lifetime. Thereafter, the extent and depth of La Niña systems drop monotonically, while the growth of El Niño systems continues until 50% of their total lifetime.

5. Precipitation Attribution

Finally, we investigate how changes in convective organization and evolution affect associated precipitation. We attribute rainfall to organized convection by collocating convective system coverage and precipitation data and taking the ratio of assigned to total rainfall for a given grid cell. We denote the resulting attribution P_{org} below and find ΔP_{org} between the warm and cold phases of ±5% over ±2-K SSTa, on the same order as the often cited 2% to 3% increase in precipitation per degree of warming (Stephens & Ellis, 2008). These values are also similar to those derived from the TRMM PR of 1.7% to 4.4% per kelvin (Wang et al., 2008). Henderson et al. (2018) have shown with 5 years of TMI retrievals, relative to radar observations at the Kwajalein Atoll, which convective rainfall tends to be underestimated (up to 30%) and stratiform overestimated (up to 33.4%) for organized convection. Although these oceanic biases of passive microwave measurements should be kept in mind, MSWEP v2.0 also incorporates reanalysis and rain gauge data. We are primarily interested in El Niño-La Niña differences in organized precipitation, so our findings should not be strongly affected.

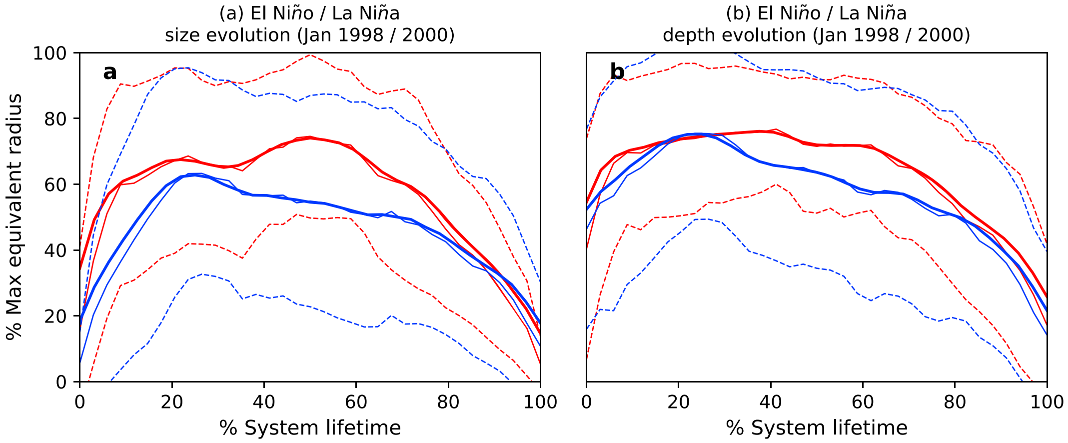

Figure 8. Normalized lifecycles for an El Niño month (red, January 1998) and a La Niña one (blue, January 2000). System equivalent radii, normalized to the maximum value, is shown in panel (a), and system cloud top temperature, normalized to the minimum value, in panel (b). The mean is shown in a thin solid line, with its 3-point running mean in a thick solid line. Plus and minus a standard deviation are shown in dashed lines.

As in the property difference climatologies, the spatial structure of warm-cold phase attribution differences ΔP_{org} (Figures 9a and 9b) is largely determined by shifts in the zonal overturning. Intensified regions of ascent over the Amazon and Maritime Continent increase P_{org} there during the cold phase. El Niño suppression of Indian monsoon rainfall during the boreal summer is also prominent. Conversely, intensified ascent over the central Pacific and Africa increase warm phase P_{org} there. Although surface moisture advection drops with weakened trade winds, the increased moisture holding capacity of overlying air during the warm phase more than compensates. Increases in P_{org}, particularly over the central Pacific, correspond closely to

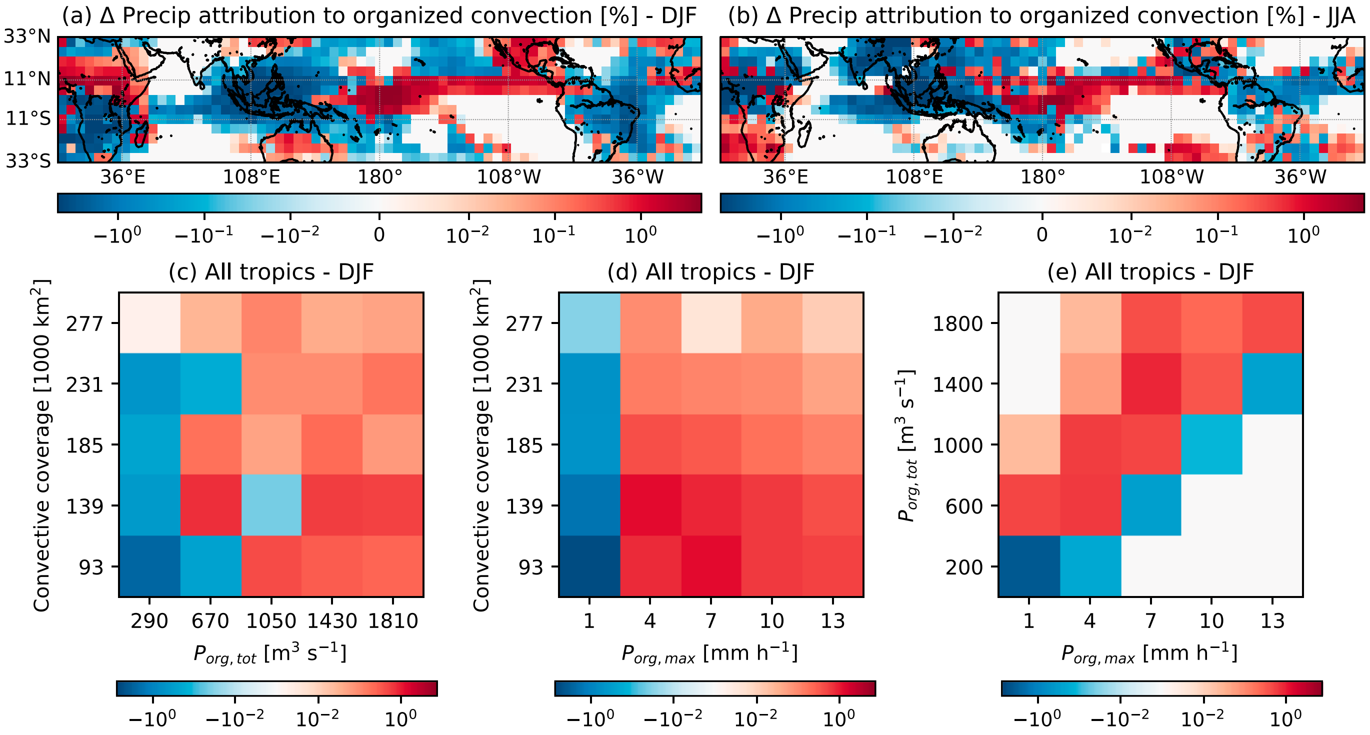

Figure 9. Changes in precipitation attributed to organized convection, P_{org}, are shown between the warm and cold phases during boreal winter and summer (a, b). Warm-cold phase differences in the joint distributions of convective system coverage and precipitation accumulation from organized systems $P_{\mathrm{org,\ tot}}$; convective system coverage and maxima from organized systems $P_{\mathrm{org,\ max}}$; and $P_{\mathrm{org,\ tot}}$ and $P_{\mathrm{org,\ max}}$ are also shown in panels (c) to (e). These are constructed for boreal winter throughout the tropics. DJF = December–February; JJA = June–August.

the increases in system occurrence (Figure 3a). The maximum increase in warm phase P_{org} also overlaps the maximum increase in system deepening and margin of largest-magnitude γ (Figure 7a). Henderson et al. (2018) have identified similar regions as being strongly affected by organized precipitation regimes during El Niño, using a combination of the TRMM TMI and PR instruments. We can use an approximate scaling of precipitation and evaporative flux area (or system coverage) to quantitatively link P_{org} back to convective structure: if precipitation attribution increases by 5% from an initial value of 30%, then the system coverage must increase by $(0.3^{-1}–0.35^{-1}) \approx 50\%$, equivalent to an 150-km increase in radius over an initial value of 250 km $((400^2–250^2)/250^2 \approx 1.5)$.

The joint distribution of system area and precipitation accumulation from organized systems $P_{\mathrm{org,\,tot}}$ indicates that larger, warm phase systems tend to bring greater volumes of rain than smaller, cold phase ones. The largest gains in $P_{\mathrm{org,tot}}$ come from systems with smaller coverage, that is, 150,000 km^2 or less ($r_{\mathrm{eq}} \leq$ 220 km). The large volume of air in more extensive systems can only generate higher $P_{\mathrm{org,\,tot}}$ up to a certain point (Zipser et al., 2006). The smaller systems also correspond to the largest differences in the maximum intensity of precipitation P_{max}. Since P_{max} is affected by moisture convergence at system margins, a lower volume-to-perimeter ratio augments $P_{\mathrm{org,\,max}}$ as long as the system is not susceptible to moisture limitation. If we instead construct joint distributions of $P_{\mathrm{org,\,tot}}$ and $P_{\mathrm{org,\,max}}$ (Figure 9e), the smaller systems during La Niña also tend to generate more intense precipitation for a given accumulation. Even in regions where occurrence and P_{org} are reduced in the cold phase, the systems that do form can be quite intense. These trends can be summarized with a dichotomy of more frequent convective organization of greater extent that brings larger volumes of precipitation during the warm phase and less numerous, less extensive systems that bring smaller volumes of precipitation during the cold phase.

6. Discussion and Conclusions

While existing research indicates that tropical cyclones intensify with El Niño or greenhouse gas (GHG) warming, we lack a basic understanding of changes with warming to convective organization at the mesoscale. Previous studies examining such changes have mostly used idealized models or regional data and have tended to focus on one aspect of these systems, their morphology, their lifecycle, or their associated precipitation. Here, we have addressed all of these elements using satellite climatologies. A recurrent theme of previous findings is the importance of interaction with larger-scale circulations, whether they be Amazonian wind shifts or mesoscale vortices (Morel & Senesi, 2002; Feng et al., 2018). In our El Niño-La Niña difference climatologies, we see an imprint of shifts in zonal overturning. The regions of greatest convective deepening are those of large-scale ascent, rather than those of warmest SSTa.

The eastward shift of zonal overturning corresponds to organized convection that is 3 times more likely and 50% larger in the central Pacific during El Niño relative to La Niña. Relative differences in depth are of smaller magnitude and more longitudinally spread, with the latter potentially reflecting the influence of large-scale wave activity. These values agree with past cloud-resolving model results that indicate wider and taller organized convection with occurrence as much as triple in a warmer future (Prein et al., 2017; Romps, 2011). The concentration of convective activity to the region of warmest SSTa reflects previous work in which the threshold temperature for convection increases with large-scale warming, suppressing convection in colder regions (Johnson & Xie, 2010; Sobel, 2010; Waliser & Gautier, 1993). The extremes of CAPE also increase during El Niño, similar to global warming projections from coarse-resolution and superparameterized global climate models (Singh & O'Gorman, 2013; Singh et al., 2017). With this increasing CAPE, the environment becomes more favorable for convective occurrence.

We can summarize the structural changes by distributional shifts in information entropy: Convective cloud fields have 20% lower entropy, or equivalently 20% more organization, during El Niño relative to La Niña. The shift is robust across a range of feature sizes from 100 km up to the entire tropics. Although simulations suggest that convective aggregation could be more likely with uniform surface warming (Coppin & Bony, 2018; Emanuel et al., 2014; Mauritsen & Stevens, 2015), this is the first study to illustrate such a shift from observations and for El Niño periods. We have also presented information about convective structure over time with a growth metric γ that quantifies the ratio of system deepening to spreading and could provide a simple means of parameterizing mesoscale convective evolution in global climate models. Large-magnitude values of γ indicate the importance of convective deepening to system growth over the warm East and central

Table 1
Summary Statistics

	WP	CP	EP	Tropics
$\overline{n}$	1,844, 3,874	2,437, 1,149	1,666, 435	59,861, 111,084
$\overline{r_{\mathrm{eq}}}$ (km)	376, 448	442, 259	209, 183	324, 301
$\partial r_{\mathrm{eq}}/\partial\mathrm{SSTa}$ (km/K)	−17.5, −23.1	20.1, −35.3	3.65, 1.0	−22, −18
$\overline{T_{\mathrm{top}}}$ (K)	189, 188	186, 196	199, 208	201, 202
$\partial T_{\mathrm{top}}/\partial\mathrm{SSTa}$	0.011, −0.093	−0.98, 1.83	0.5, 0.28	0.18, 0.12
$\overline{H}$	—	—	—	0.238, 0.293
$\overline{\gamma}$	−0.0088, −0.0089	−0.0094, −0.0093	−0.0131, −0.0138	−0.0093, −0.0105
$\overline{\Delta P_{\mathrm{org}}}$	−2.0%	+4.07%	+0.34%	−0.35%

Note. For each value and subdomain, the El Niño value is listed first followed by the La Niña one. Mean occurrence $\overline{n}$, horizontal extent $\overline{r_{\mathrm{eq}}}$, SSTa dependence of extent $\partial r_{\mathrm{eq}}/\partial\mathrm{SSTa}$, vertical depth $\overline{T_{\mathrm{top}}}$, SSTa dependence of depth $\partial T_{\mathrm{top}}/\partial\mathrm{SSTa}$, entropy $\overline{H}$, growth metric $\overline{\gamma}$, and EN-LN precipitation attribution difference $\overline{\Delta P_{\mathrm{org}}}$ for West Pacific (WP: 5°S to 5°N, 125–155°E), central Pacific (CP: 5°S to 5°N, 165°E to 165°W), East Pacific (EP: 5°S to 5°N, 115–145°W), and tropics-wide domains.

Pacific waters during El Niño, while small-magnitude values of γ reflect the importance of spreading to growth in the cooler West Pacific.

In the regions where convective organization is more frequent and more extensive during El Niño, attributable precipitation goes up by as much as 5%. Precipitation increases over recent decades have been attributed to higher frequency of organized convection, also using ISCCP data (Tan et al., 2015). Despite differences in modes of warming, these values quantitatively follow past modeling studies on larger domains for which a degree kelvin warming translates to about a 2% increase in rainfall (Muller et al., 2011; Romps, 2011; Stephens & Ellis, 2008). Relative to regional studies, however, such as those of Anderson and Arritt (2001) or Prein et al. (2017) over the continental United States, we tend to see smaller increases in attributable precipitation with warming. We find that convective systems generate larger precipitation accumulations $P_{\mathrm{org,\,tot}}$ during El Niño with the biggest gains from smaller systems, similar to joint distributions of system size and precipitation volume in Prein et al. (2017). For a given system size, the precipitation also tends to be more intense during El Niño (larger $P_{\mathrm{org,\,max}}$), while for a given precipitation accumulation, the precipitation is actually more intense during La Niña. These trends, along with larger tropics-wide values of γ, suggest that systems deepen and decay more rapidly during La Niña. On the basis of TMI and PR data, Henderson et al. (2018) also showed recently a shift from isolated deep convection in La Niña to greater organization in El Niño. Using exclusively precipitation data, they found increased areal coverage, tropospheric deepening, and largest effects in the Pacific during El Niño, similar to results that we have shown here. We summarize these quantitatively in Table 1.

Our findings on precipitation accumulation and intensity will also be affected by the speed at which convective systems propagate, an effect that we have not explored here. ENSO variability seems to be increasing as climate warms, mostly due to augmented land-ocean contrasts (Fasullo et al., 2018). These contrasts should strengthen the climatological patterns we see already, particularly over the continents. The questions of how El Niño flavor or the increasing propensity for central Pacific El Niño affects the results here should also be considered going forward. More generally, global climate model simulations suggest that the future climate under GHG forcing, especially that of the tropical Pacific, will shift toward a more El Niño-like state (Cai et al., 2014; Timmermann et al., 1999; Wang et al., 2017). SST patterns from anthropogenic warming and El Niño do not align exactly (Xie et al., 2010); in particular, the larger extent of positive SSTa under GHG than ENSO warming may diminish the continental moisture limitations mentioned above. In this case, the evolution of convective organization looks more like the central Pacific picture everywhere, with larger systems that bring bigger volumes of rain. Our future work will focus on relating convective depth and precipitation intensity, as well as more rigorously attributing convective enlargement to thick versus thin cirrus anvil. These links of precipitation and radiation to convection are crucial to understand, as their coupling determines the tropical climate sensitivity.

Acknowledgments
This work was partially supported by NSF Grant GG012658-01. ISCCP data are publicly available online (https://earth.ccny.cuny.edu/rscg/hdata/index.php?dir=ct). Work by K.A.S. was carried out at the Jet Propulsion Laboratory, California Institute of Technology, under a contract with the National Aeronautics and Space Administration. Thanks to ECMWF and Hylke Beck at Princeton University for providing meteorological and precipitation data; these data sets are available at https://www.ecmwf.int/en/forecasts/datasets/archive-datasets/reanalysis-datasets/era-interim and http://www.gloh2o.org/ websites. We have also made our scripts for collocation of MCS and meteorological values or precipitation available at the website (http://sylviacsullivan.wixsite.com/info/codes-and-slides). We thank Brahim Khalil Abid for initial organization of the convective tracking database and three reviewers for thorough and insightful feedback. S. C. S. acknowledges Sandrine Bony and Jean-Philippe Duvel for thought-provoking discussion of the climatologies and Fabio d'Andrea, Paolo Davini, Sara Shamekh, and Caroline Muller for discussion of metrics of convective organization.

References

Alcantara, C. R., Dias, M. A. F. S., Souza, E. P., & Cohen, J. C. P. (2011). Verification of the role of the low level jets in Amazon squall lines. *Atmospheric Research*, *100*, 36–44. https://doi.org/10.1016/j.atmosres.2010.12.023

Allen, M. R., & Ingram, W. J. (2002). Constraints on future changes in climate and the hydrologic cycle. *Nature*, *419*, 224–232.

Anber, U., Wang, S., & Sobel, A. H. (2015). Effect of surface fluxes versus radiative heating on tropical deep convection. *Journal of the Atmospheric Sciences*, *72*, 3378–3388. https://doi.org/10.1175/JAS-D-14-0253.1

Anderson, C. J., & Arritt, R. W. (2001). Mesoscale convective systems over the United States during the 1997–98 El Niño. *Monthly Weather Review*, *129*, 2443–2457. https://doi.org/10.1175/1520-0493(2001)129-2443:MCSOTU2.0.CO;2

Arnaud, Y., Desbois, M., & Maizi, J. (1992). Automatic tracking and characterization of African convective systems on Meteosat pictures. *Monthly Weather Review*, *31*(5), 443–453.

Bao, J., Sherwood, S. C., Alexander, L. V., & Evans, J. P. (2017). Future increases in extreme precipitation exceed observed scaling rates. *Nature Climate Change*, 128–133. https://doi.org/10.1038/nclimate3201

Beck, H. E., van Dijk, A. I. J. M., Levizzani, V., Schellekens, J., Miralles, D. G., Martens, B., & de Roo, A. (2017). MSWEP: 3-hourly 0.25-degree global gridded precipitation (1979–2015) by merging gauge, satellite, and reanalysis data. *Hydrology and Earth System Sciences*, *21*, 589–615. https://doi.org/10.5194/hess-21-589-2017

Beck, H. E., Vergopolan, N., Pan, M., Levizzani, V., van Dijk, A. I. J. M., Weedon, G. P., et al. (2017). Global-scale evaluation of 22 precipitation datasets using gauge observations and hydrological modeling. *Hydrology and Earth System Sciences*, *21*, 6201–6217. https://doi.org/10.5194/hess-21-6201-2017

Becker, T., Bretherton, C. S., Hohenegger, C., & Stevens, B. (2018). Estimating bulk entrainment with unaggregated and aggregaed convection. *Geophysical Research Letters*, *45*, 455–462. https://doi.org/10.1002/2017GL076640

Bony, S., Stevens, B., Coppin, D., Becker, T., Reed, K. A., Voigt, A., & Medeiros, B. (2017). Thermodynamic control of anvil cloud amount. *Proceedings of the National Academy of Sciences*, *113*(32), 8927–8932. https://doi.org/10.1073/pnas.1601472113

Bouniol, D., Roca, R., Fiolleau, T., & Poan, D. E. (2016). Macrophysical, microphysical, and radiative properties of tropical mesoscale convective systems over their life cycle. *Journal of Climate*, *29*, 3353–3371. https://doi.org/10.1175/JCLI-D-15-0551.1

Cai, W., Borlace, S., Lengaigne, M., van Rensch, P., Collins, M., Vecchi, G., et al. (2014). Increasing frequency of extreme El Niño events due to greenhouse warming. *Nature Climate Change*, *4*, 111–116. https://doi.org/10.1038/nclimate2100

Chahine, M. T., Pagano, T. S., Aumann, H. H., Atlas, R., Barnet, C., Blaisdell, J., et al. (2006). AIRS: Improving weather forecasting and providing new data on greenhouse gases. *Bulletin of the American Meteorological Society*, *87*, 911–926. https://doi.org/10.1175/BAMS-87-7-911

Chakraborty, S., Fu, R., Massie, S. T., & Stephens, G. (2016). Relative influence of meteorological conditions and aerosols on the lifetime of mesoscale convective systems. *Proceedings of the National Academy of Sciences*. https://doi.org/10.1073/pnas.1601935113

Chiang, J. C. H., & Sobel, A. H. (2002). Tropical tropospheric temperature variations caused by ENSO and their influence on the remote tropical climate. *Journal of Climate*, *15*, 2616–2631. https://doi.org/10.1175/1520-0442(2002)015-2616:TTTVCB-2.0.CO;2

Chou, C., Chiang, J. C. H., Lan, C.-W., Chung, C.-H., Liao, Y.-C., & Lee, C.-J. (2013). Increase in the range between wet and dry season precipitation. *Nature Geoscience*, *6*, 263–267. https://doi.org/10.1038/ngeo1744

Coppin, D., & Bony, S. (2018). On the interplay between convective aggregation, surface temperature gradients, and climate sensitivity. *Journal of Advances in Modeling Earth Systems*, *10*, 3123–3138. https://doi.org/10.1029/2018MS001406

Dee, D. P., Uppala, S. M., Simmons, A. J., Berrisofrd, P., Poli, P., Kobayashi, S., et al. (2011). The ERA-Interim reanalysis: Configuration and performance of the data assimilation system. *Quarterly Journal of the Royal Meteorological Society*, *137*, 553–597. https://doi.org/10.1002/qj.828

Elsaesser, G. S., & Kummerow, C. D. (2010). A multisensor observational depiction of the transition from light to heavy rainfall on subdaily time scales. *Journal of the Atmospheric Sciences*, *70*, 2309–2324. https://doi.org/10.1175/JAS-D-12-0210.1

Emanuel, K. (2005). Increasing destructiveness of tropical cyclones over the past 30 years. *Nature*, *436*, 686–688. https://doi.org/10.1038/nature03906

Emanuel, K., Wing, A. A., & Vincent, E. M. (2014). Radiative-convective instability. *Journal of Advances in Modeling Earth Systems*, *6*, 75–90. https://doi.org/10.1002/2013MS000270

Fasullo, J. T., Otto-Bliesner, B. L., & Stevenson, S. (2018). ENSO's changing influence on temperature, precipitation, and wildfire in a warming climate. *Geophysical Research Letters*, *45*, 9216–9225. https://doi.org/10.1029/2018GL079022

Feng, Z., Leung, L. R., Hago, S., Houze, R. A., Burleyson, C. D., & Balaguru, K. (2016). More frequent intense and long-lived storms dominate the springtime trend in central US rainfall. *Nature Communications*, *7*(13429). https://doi.org/10.1038/ncomms13429

Feng, Z., Leung, L. R., Houze, R. A., Hagos, S., Hardin, J., Yang, et al. (2018). Structure and evolution of mesoscale convective systems: Sensitivity to cloud microphysics in convection-permitting simulations over the United States. *Journal of Advances in Modeling Earth Systems*, *10*, 1470–1494. https://doi.org/10.1029/2018MS001305

Fiolleau, T., & Roca, R. (2013). An algorithm for the detection and tracking of tropical mesoscale convective systems using infrared images from geostationary satellites. *IEEE Transactions on Geoscience and Remote Sensing*, *51*(7), 4302–4315.

Fischer, E. M., & Knutti, R. (2016). Observed heavy precipitation increase confirms theory and early models. *Nature Climate Change*, *6*, 986–991. https://doi.org/10.1038/nclimate3110

Funk, C., Peterson, P., Landsfeld, M., Pedreros, D., Verdin, J., Shukla, S., et al. (2015). The climate hazards infrared precipitation with stations—A new environmental record for monitoring extremes. *Scientific Data*, *2*, 150066. https://doi.org/10.1038/sdata.2015.66

Goyens, C., Lauwaet, D., Schröder, M., Demuzere, M., & Lipzig, N. P. M. V. (2011). Tracking mesoscale convective systems in the Sahel: Relation between cloud parameters and precipitation. *International Journal of Climatology*, *32*(12), 1921–1934. https://doi.org/10.1002/joc.2407

Hagos, S., Feng, Z., McFarlane, S., & Leung, L. R. (2013). Environment and the lifeime of tropical deep convection in a cloud-permitting regional model simulation. *Journal Atmospheric Sciences*, *70*, 2409–2425. https://doi.org/10.1175/JAS-D-12-0260.1

Hameed, S. N., Jin, D., & Thilakan, V. (2018). A model for super El Niños. *Nature Communications*, *9*(2528). https://doi.org/10.1038/s41467-018-04803-7

Hartmann, D. L., & Larson, K. (2002). An important constraint on tropical cloud-climate feedback. *Geophysical Research Letters*, *29*(20), 1951. https://doi.org/10.1029/2002GL015835

Hasino, T., Satoh, M., Hagihara, Y., Kubota, T., Matsui, T., Nasuno, T., & Okamoto, H. (2013). Evaluating cloud microphysics from NICAM against CloudS at and CALIPSO. *Journal of Geophysical Research: Atmospheres*, *118*, 7473–7292. https://doi.org/10.1002/jgrd.50564

Held, I. M., & Zhao, M. (2011). The response of tropical cyclone statistics to an increase in CO_2 with fixed sea surface temperatures. *Journal of Climate*, *24*, 5353–5364. https://doi.org/10.1175/JCLI-D-11-00050.1

Henderson, D. S., Kummerow, C. D., & Berg, W. (2018). ENSO influence on TRMM tropical oceanic precipitation characteristics and rain rates. *Journal of Climate*, *31*, 3979–3998. https://doi.org/10.1175/JCLI-D-17-0276.1

Henderson, D. S., Kummerow, C. D., Marks, D. A., & Berg, W. (2017). A regime-based evaluation of TRMM oceanic precipitation biases. *Journal of Atmospheric and Oceanic Technology*, *34*, 2613–2635. https://doi.org/10.1175/JTECH-D-16-0244.1

Holloway, C. E., Wing, A. A., Bony, S., Muller, C., Masunaga, H., & L'Ecuyer, T. S. (2017). Observing convective aggregation. *Surveys in Geophysics*, *38*(6), 1199–1236. https://doi.org/10.1007/s10712-017-9419-1, http://link.springer.com/10.1007/s10712-017-9419-1

Houze, R. A. (2004). Mesoscale convective systems. *Reviews of Geophysics*, *42*, RG4003. https://doi.org/10.1029/2004RG000150

Houze, R. A., Wilton, D. C., & Smull, B. F. (2007). Monsoon convection in the Himalayan region as seen by the TRMM precipitation radar. *Quarterly Journal of the Royal Meteorological Society*, *133*(627), 1389–1411. https://doi.org/10.1002/qj.106

Johnson, R. H., Rickenbach, T. M., Rutledge, S. A., Ciesielski, P. E., & Schubert, W. H. (1999). Trimodal characteristics of tropical convection. *Journal of Climate*, *12*, 2397–2418. https://doi.org/10.1175/1520-0442(1999)0122397:TCOTC2.0.CO;2

Johnson, N. C., & Xie, S.-P. (2010). Changes in the sea surface temperature threshold for tropical convection. *Nature Geoscience*, *3*, 842–845.

Kidd, C., Bauer, P., Turk, J., Huffman, G. J., Joyce, R., Hsu, K.-L., & Braithwaite, D. (2012). Intercomparison of high-resolution precipitation products over Northwest Europe. *Journal of Hydrometeorology*, *13*, 67–83. https://doi.org/10.1175/JHM-D-11-042.1

Kidd, C., Becker, A., Huffmann, G. J., Muller, C. L., Joe, P., Skofronick-Jackson, G., & Kirschbaum, D. B. (2017). So, how much of the Earth's surface is covered by rain gauges? *Bulletin of the American Meteorological Society*, *98*, 69–78. https://doi.org/10.1175/BAMS-D-14-00283.1

Kidder, S. Q., & Haar, T. H. V. (1995). *Satellite meteorology: An introduction* (pp. 79). San Diego: Elsevier.

Kim, H.-M., Zhou, Y., & Alexander, M. A. (2017). Changes in atmospheric rivers and moisture transport over the Northeast pacific and western North America in response to ENSO diversity. *Climate Dynamics*. https://doi.org/10.1007/s00382-017-3598-9

Klocke, D., Brueck, M., Hohenegger, C., & Stevens, B. (2017). Rediscovery of the doldrums in storm-resolving simulations over the tropical Atlantic. *Nature Geoscience*, *10*, 891–896. https://doi.org/10.1038/s41561-017-0005-4

Knutson, T. R., & Tuleya, R. E. (2004). Impact of CO_2-induced warming on simulated hurricane intensity and precipitation: Sensitivity to the choice of climate model and convective parameterization. *Journal of Climate*, *17*(18), 3477–3495.

Kuang, Z. (2007). A moisture-stratiform instability for convectively coupled waves. *Journal of the Atmospheric Sciences*, *65*, 834–854. https://doi.org/10.1175/2007JAS2444.1

Lau, W. M., & Zhou, Y. P. (2012). Observed recent trends in tropical cyclone rainfall over the North Atlantic and North Pacific. *Journal of Geophysical Research*, *117*, D03104. https://doi.org/10.1029/2011JD016510

Laurent, H., Machado, L. A. T., Morales, C. A., & Durieux, L. (2002). Characteristics of the Amazonian mesoscale convective systems observed from satellite and radar during the WETAMC/LBA experiment. *Journal of Geophysical Research*, *107*(D20), LBA 21–1–LBA 21–17. https://doi.org/10.1029/2001JD000337

Li, Y., Yang, P., North, G. R., & Dessler, A. (2012). Test of the fixed anvil temperature hypothesis. *Journal of the Atmospheric Sciences*, *69*, 2317–2328. https://doi.org/10.1175/JAS-D-11-0158.1

Lindzen, R. S., Chou, M.-D., & Hou, A. U. (2001). Does the Earth have an adaptive infrared iris? *Bulletin of the American Meteorological Society*, *82*, 417–432. https://doi.org/10.1175/1520-0477(2001)0820417:DTEHAA2.3.CO;2

Machado, L. A. T., Desbois, M., & Duvel, J.-P. (1992). Structural characteristics of deep convective systems over tropical Africa and Atlantic Ocean. *Monthly Weather Review*, *120*, 392–406.

Machado, L. A. T., & Rossow, W. B. (1993). Structural characteristics and radiative properties of tropical cloud clusters. *Monthly Weather Review*, *121*, 3234–3260. https://doi.org/10.1175/1520-0493-281993-29121-3234-3ASCARPO-2.0.CO-3B2

Machado, L. A. T., Rossow, W. B., Guedes, R. L., & Walker, A. W. (1998). Life cycle variations of mesoscale convective systems over the Americas. *Monthly Weather Review*, *126*, 1630–1654. https://doi.org/10.1175/1520-0493(1998)1261630:LCVOMC2.0.CO;2

Mapes, B., Milliff, R., & Morzel, J. (2009). Composite life cycle of maritime tropical mesoscale convective systems in scatterometer and microwave satellite observations. *Journal of the Atmospheric Sciences*, *66*, 199–208. https://doi.org/10.1175/2008JAS2746.1

Masunaga, H., L'Ecuyer, T. S., & Kummerow, C. D. (2005). Variability in the characteristics of precipitation systems in the tropical Pacific. Part I: Spatial structure. *Journal of Climate*, *18*, 823–840. https://doi.org/10.1175/JCLI-3304.1

Mauritsen, T., & Stevens, B. (2015). Missing iris effect as a possible cause of muted hydrological change and high climate sensitivity in models. *National Geographic*, *8*, 346–351. https://doi.org/10.1038/ngeo2414

Morel, C., & Senesi, S. (2002). A climatology of mesoscale convective systems over Europe using satellite infrared imagery. II: Characteristics of European mesoscale convective systems. *Quarterly Journal of the Royal Meteorological Society*, *128*, 1973–1995. https://doi.org/10.1256/003590002320603494

Muller, C. (2013). Impact of convective organization on the response of tropical precipitation extremes to warming. *Journal of Climate*, *26*, 5028–5043. https://doi.org/10.1175/JCLI-D-12-00655.1

Muller, C. J., O'Gorman, P. A., & Back, L. E. (2011). Intensification of precipitation extremes with warming in a cloud-resolving model. *Journal of Climate*, *24*, 2784–2800. https://doi.org/10.1175/2011JCLI3876.1

Nesbitt, S. W., & Zipser, E. J. (2003). The diurnal cycle of rainfall and convective intensity according to three years of TRMM measurements. *Journal of Climate*, *16*, 1456–1475. https://doi.org/10.1175/1520-0442-16.10.1456

Park, H.-S., & Chiang, J. C. H. (2010). The delayed effect of major El Niño events on Indian monsoon rainfall. *Journal of Climate*, *23*, 932–946. https://doi.org/10.1175/2009JCLI2916.1

Prein, A. F., Liu, C., Ikeda, K., Trier, S. B., Rasmussen, R. M., Holland, G. J., & Clark, M. P. (2017). Increased rainfall volume from future convective storms in the US. *Nature Climate Change*, *7*, 880–884. https://doi.org/10.1038/s41558-017-0007-7

Prein, A. F., Rasmussen, R. M., Ikeda, K., Liu, C., & Clark, M. P. (2016). The future intensification of hourly precipitation extremes. *Nature Climate Change*, *7*, 48–53. https://doi.org/10.1038/nclimate3168

Protopapadaki, E.-S., Stubenrauch, C. J., & Feofilov, A. (2017). Upper tropospheric cloud systems derived from IR sounders: Properties of cirrus anvils in the tropics. *Atmospheric Chemistry and Physics*, *17*, 3845–3859. https://doi.org/10.5194/acp-173845-2017

Punkka, A.-J., & Bister, M. (2015). Mesoscale convective systems and their synoptic scale environment in Finland. *Weather and Forecasting*, *30*, 182–196. https://doi.org/10.1175/WAF-D-13-00146.1

Ricciardulli, L., & Sardeshmukh, P. (2002). Local time- and space scales of organized tropical deep convection. *Journal of Climate*, *15*, 2775–2790. https://doi.org/10.1175/1520-0442(2002)0152775:LTASSO2.0.CO;2

Roca, R., Aublanc, J., Chambon, P., Fiolleau, T., & Viltard, N. (2014). Robust observational quantification of the contribution of mesoscale convective systems to rainfall in the tropics. *Journal of Climate*, *27*, 4952–4958. https://doi.org/10.1175/JCLI-D-13-00628.1

Roca, R., Fiolleau, T., & Bouniol, D. (2017). A simple model of the life cycle of mesoscale convective systems cloud shield in the tropics. *Journal of Climate*, *30*, 4283–4298. https://doi.org/10.1175/JCLI-D-16-0556.1

Romps, D. (2011). Response of tropical precipitation to global warming. *Journal of the Atmospheric Sciences*, *68*, 123–138. https://doi.org/10.1175/2010JAS3542.1

Romps, D. (2014). An analytical model for tropical relative humidity. *Journal of the Atmospheric Sciences*, *27*, 7432–7449. https://doi.org/10.1175/JCLI-D-14-00255.1

Rossow, W. B., Mekonnen, A., Pearl, C., & Goncalves, W. (2013). Tropical precipitation extremes. *Journal of Climate*, *26*, 1457–1466. https://doi.org/10.1175/JCLI-D-11-00725.1

Rossow, W. B., & Schiffer, R. A. (1999). Advances in understanding clouds from ISCCP. *Bulletin of the American Meteorological Society*, *66*, 1498–1505.

Rossow, W. B., Walker, A. W., Beuschel, D., & Roiter, M. (1996). International Satellite Cloud Climatology Project (ISCCP): Description of new cloud datasets. *WMO/TD World Climate Research Programme (ICSU and WMO)*, *737*, 115.

Schumacher, C., Houze, R. A., & Kraucunas, I. (2004). The tropical dynamical response to latent heating estimates derived from the TRMM precipitation radar. *Journal of Climate*, *61*, 1341–1358. https://doi.org/10.1175/1520-0469(2004)061341:TTDRTL2.0CO;2

Seeley, J. T., Jeevanjee, N., & Romps, D. M. (2019). FAT or FiTT: Are anvil clouds or the tropopause temperature invariant? *Geophysical Research Letters*, *46*, 1842–1850. https://doi.org/10.1029/2018GL080095

Sherwood, S. C., Minnis, P., McGill, M., & Chae, J. C. (2004). Underestimation of deep convective cloud tops by thermal imagery. *Geophysical Research Letters*, *31*, L11102. https://doi.org/10.1029/2004GL019699

Singh, M. S., Kuang, Z., Maloney, E. D., Hannah, W. M., & Wolding, B. O. (2017). Increasing potential for intense tropical and subtropical thunderstorms under global warming. *Proceedings of the National Academy of Sciences*, *114*(44), 11,657–11,662. https://doi.org/10.1073/pnas.1707603114

Singh, M. S., & O'Gorman, P. A. (2013). Influence of entrainment on the thermal stratification in simulations of radiative-convective equilibrium. *Geophysical Research Letters*, *40*, 4398–4403. https://doi.org/10.1002/grl.50796

Singleton, A., & Toumi, R. (2013). Super-Clausius-Clapeyron scaling of rainfall in a model squall line. *Quarterly Journal of the Royal Meteorological Society*, *139*, 334–339.

Sobel, A. (2010). Raised bar for rain. *Nature Geoscience*, *3*, 821–822. https://doi.org/10.1038/ngeo1025

Stensrud, D. J. (1996). Importance of low-level jets to climate: A review. *Journal of Climate*, *9*, 1698–1711. https://doi.org/10.1175/1520-0442(1996)0091698:IOLLJT2.0.CO;2

Stephens, G. L., & Ellis, T. D. (2008). Controls of global-mean precipitation increases in global warming GCM experiments. *Journal of Climate*, *21*, 6141–6155. https://doi.org/10.1175/2008JCLI2144.1

Stephens, G. L., Hakuba, M. Z., Webb, M. J., Lebsock, M., Yue, Q., Kahn, B. H., et al. (2018). Regional intensification of the tropical hydrological cycle during ENSO. *Geophysical Research Letters*, *45*, 4361–4370. https://doi.org/10.1029/2018GL077598

Stubenrauch, C. J., Rossow, W. B., Kinne, S., Ackerman, S., Cesana, G., Chepfer, H., et al. (2013). Assessment of the global cloud datasets from satellites: Project and database initiated by the GEWEX radiation panel. *Bulletin of the American Meteorological Society*, *94*, 1031–1049. https://doi.org/10.1175/BAMS-D-12-00117.1

Sun, Q., Miao, C., Duan, Q., Ashouri, H., Sorooshian, S., & Hsu, K.-L. (2017). A review of global precipitation data sets: Data sources, estimation, and intercomparisons. *Reviews of Geophysics*, *56*, 79–107. https://doi.org/10.1002/2017RG000574

Tan, J., Jakob, C., Rossow, W. B., & Tselioudis, G. (2015). Increases in tropical rainfall driven by changes in frequency of organized deep convection. *Nature*, *519*, 451–454. https://doi.org/10.1038/nature14339

Tao, W.-K., & Chern, J.-D. (2017). The impact of simulated mesoscale convective systems on global precipitation: A multiscale modeling study. *Journal of Advances in Modeling Earth Systems*, *9*, 790–809. https://doi.org/10.1002/2016MS000836

Timmermann, A., Oberhuber, J., Bacher, A., Esch, M., Latif, M., & Roeckner, E. (1999). Increased El Niño frequency in a climate model forced by future greenhouse warming. *Nature*, *398*, 694–697. https://doi.org/10.1038/19505

Tompkins, A., & Craig, G. C. (1999). Sensitivity of tropical convection to sea surface temperature in the absence of large-scale flow. *Journal of Climate*, *12*, 462–276. https://doi.org/10.1175/1520-0442(1999)0120462:SOTCTS2.0.CO;2

Tsakraklides, G., & Evans, J. L. (2003). Global and regional diurnal variations of organized convection. *Journal of Climate*, *16*, 1562–1572. https://doi.org/10.1175/1520-0442-16.10.1562

Vant-Hull, B., Rossow, W., & Pearl, C. (2016). Global comparisons of regional life cycle properties and motion of multiday convective systems: Tropical and midlatitude land and ocean. *Journal of Climate*, *29*, 5837–5858. https://doi.org/10.1175/JCLI-D-15-0698.1

Vernekar, A. D., Kirtman, B. P., & Fennessy, M. J. (2003). Low-level jets and their effects on the South American summer climate as simulated by the NCEP Eta model. *Journal of Climate*, *16*, 297–311. https://doi.org/10.1175/1520-0442(2003)0160297:LLJATE2.0.CO;2

Waliser, D. E., & Gautier, C. (1993). A satellite-derived climatology of the ITCZ. *Journal of Climate*, *6*, 2162–2174. https://doi.org/10.1175/1520-0442(1993)0062162%3AASDCOT2.0.CO%3B2

Wall, C. J., Hartmann, D., Thieman, M., Smith, W. J., & Minnis, P. (2018). The lifecycle of anvil clouds and the top-of-atmosphere radiation balance over the tropical West Pacific. *Journal of Climate*, *31*, 10,059–10,080. https://doi.org/101175/JCLI-D-18-0154.1

Wang, J.-J., Adler, R. F., & Gu, G. (2008). Tropical rainfall-surface temperature relations using Tropical Rainfall Measuring Mission precipitation data. *Journal of Geophysical Research*, *113*, D18115. https://doi.org/10.1029/2007JD009540

Wang, G., Cai, W., Gan, B., Wu, L., Santoso, A., Lin, X., et al. (2017). Continued increase of extreme El Niño frequency long after 1.5 °C warming stabilization. *Nature Climate Change*, *7*, 568–573. https://doi.org/10.1038/nclimate3351

Wielicki, B. A., & Welch, R. M. (1986). Cumulus cloud properties derived using Landsat satellite data. *Journal of Climate and Applied Meteorology*, *25*(3), 261–276.

Williams, M., & Houze, R. A. (1987). Satellite-observed characteristics of winter monsoon cloud clusters. *Monthly Weather Review*, *115*, 505–519.

Wolter, K., & Timlin, M. S. (2011). El niño/Southern Oscillation behaviour since 1871 as diagnosed in an extended multivariate ENSO index (MEI.ext). *International Journal of Climatology*, *31*, 1074–1087. https://doi.org/10.1002/joc.2336

Xie, S.-P., Deser, C., Vecchi, G. A., Ma, J., Teng, H., & Wittenberg, A. T. (2010). Global warming pattern formation: Sea surface temperature and rainfall. *Journal of Climate*, *23*, 966–986. https://doi.org/10.1175/2009JCLI3329.1

Yuan, J., & Houze, R. A. (2010). Global variability of mesoscale convective system anvil structure from A-train satellite data. *Journal of Climate*, *23*, 5864–5888. https://doi.org/10.1175/2010JCLI3671.1

Zelinka, M. D., & Hartmann, D. L. (2010). Why is longwave cloud feedback positive? *Journal of Geophysical Research*, *115*, D16117. https://doi.org/10.1029/2010JD013817

Zipser, E. J., Cecil, D. J., Liu, C., Nesbitt, S. W., & Yorty, D. P. (2006). Where are the most intense thunderstorms on Earth? *Bulletin of the American Meteorological Society*, *87*, 1057–1071. https://doi.org/10.1175/BAMS-87-8-1057